NTNU
Norwegian University of
Science and Technology

Power production experiments at the Test Beam Line in the CLIC Test Facility 3

Reidar Lunde Lillestøl

CERN-THESIS-2010-246
21/12/2010

Master of Science in Electronics
Submission date: December 2010
Supervisor: Lars Magne Lundheim, IET

Norwegian University of Science and Technology
Department of Electronics and Telecommunications

Problem Description

The project suggested concerns accelerator research related to the CLIC study [1]. CLIC is a study for a future Multi-TeV electron-positron collider, and is a candidate for the machine which will follow the LHC in high-energy particle physics experiments. CLIC is based on a novel particle acceleration concept, where the power needed to accelerate the particles to be collided is extracted from a high intensity electron drive beam.

At CERN, as part of the CLIC Test Facility 3 (CTF3) [2], the Test Beam Line experiment (TBL) [3] is currently under construction, and will provide the first proof of principle of stable energy extraction from a high intensity drive beam. A number of power extraction and transfer structures (PETS) will extract a large fraction of the energy from the CTF3 drive beam, and in the process the energy extracted is converted into radio-frequency (rf) power at a frequency of 12 GHz. Measurement and analysis of the TBL rf power will therefore be a key part of the TBL experiments.

The rf power production in a PETS can be predicted from PETS design parameters and drive beam parameters. Furthermore, the 12 GHz power production mode has the characteristics that the amplitude of the field is independent of the drive beam offset with respect to the structure axis, in an ideally constructed PETS. An experiment is planned where the correlation between the drive beam offset and the rf power production will be investigated. The student will take responsibility for performing this experiment, and he has to measure the produced 12 GHz power as a function of beam position and compare with theory. Therefore he needs to measure the ingoing beam parameters and the rf power produced. Rf power measurement as well as beam offsets have to be calibrated. The student must be able to easily operate the hardware of the TBL (magnetic elements and beam position monitors) in order to efficiently measure an eventual correlation. The tasks of the student will include development of data acquisition and GUI software for various TBL measurements (including PETS rf signals and beam position monitor signals), and the software developed will serve to facilitate the operation of the TBL.

It is as well of interest to benchmark the absolute value of the power measurements with the calculated predictions. The student will also participate in this work, including learning how to handle specialized beam instrumentation for measuring bunch energy, bunch length and bunch frequency. However, the accuracy of this benchmarking will be subject to the available instrumentation as well as available drive beam time for the TBL.

The test beam line, was partially commissioned last year, and the first PETS (out of 16) is installed, equipped with two rf output couplers. Starting summer 2010, further commissioning of the Test Beam Line will take place. The correlation experiments, using the first PETS, are planned to be performed during late summer or autumn 2010.

References:
[1] The CLIC Study Team, "A 3 TeV e+e- Linear Collider Based on CLIC Technology", 2000
[2] G. Geschonke and A. Ghigo (eds.), CTF3 Design Report , CERN, Geneva, 2002
[3] E. Adli et al., "Experimental Program for the CLIC Test Facility 3 Test Beam line", Presented at the First International Particle Accelerator Conference, IPAC'10, Kyoto, Japan, 2010

Assignment given: 06. July 2010
Supervisor: Lars Magne Lundheim, IET

Abstract

CLIC is an international study of a future multi-TeV electron-positron linear collider, where the energy of a high-intensity drive beam is extracted and transferred to the main beam via Power Extraction and Transfer Structures (PETS) in the form of rf power. The study of power production is therefore essential for the feasibility of CLIC. Power production in PETS has been studied, and experiments have been performed in the decelerator Test Beam Line in the CLIC Test Facility 3.

In particular, the correlation of the power production and the beam position inside the structure has been studied. It is shown that the total produced power is constant when the beam has a position offset through the PETS. In addition, the difference between the measured phases from each side is independent of the beam position, which allows for efficient combination of the fields. However, the ratio of the power on each side of the PETS unexpectedly shows a linear dependence on the horizontal offset, with a correlation value of 0.87. This can potentially affect the power transferred to the main linac, and should be taken into account in the design of the high power rf system.

A graphical user interface was developed for the Test Beam Line, and the functionality is described in detail. The program is used in the operation of the Test Beam Line for monitoring, matching, steering and power production experiments, and has interfaces to MAD-X and PLACET. A documentation is also given of the Test Beam Line and the methods of the power measurements.

Contents

1 Introduction **1**
- 1.1 About CERN . . . 1
- 1.2 Looking towards the future . . . 2
- 1.3 Outline of the thesis . . . 3
- 1.4 Acknowledgements . . . 4

2 Accelerator physics **5**
- 2.1 Dynamics of charged particle beams . . . 5
  - 2.1.1 Basic principles . . . 5
  - 2.1.2 Magnet types . . . 6
  - 2.1.3 Particle trajectories and transfer matrices . . . 8
  - 2.1.4 Phase space, emittance and the Twiss parameters . . . 9
  - 2.1.5 Matching of beam optics . . . 11
- 2.2 Wakefields . . . 12
- 2.3 RF systems for particle acceleration . . . 14
  - 2.3.1 Resonant standing wave cavities . . . 14
  - 2.3.2 Travelling wave accelerating structures . . . 15
- 2.4 Beam current and time structure . . . 16
- 2.5 Beam diagnostics . . . 17
  - 2.5.1 Beam position monitors . . . 18
  - 2.5.2 Spectrometers . . . 19
  - 2.5.3 Quad scans . . . 20
- 2.6 Beam steering . . . 21
- 2.7 Rf power generation in PETS . . . 22
  - 2.7.1 Power extraction . . . 23
  - 2.7.2 Beam deceleration . . . 26

3 The Test Beam Line **27**
- 3.1 The CLIC Test Facility 3 . . . 27
- 3.2 The TBL baseline . . . 28
- 3.3 Current status . . . 30
- 3.4 Methods of power measurements . . . 31
  - 3.4.1 Calibration of the IQ demodulator . . . 33

4 The TBL graphical user interface **34**
- 4.1 Optics, matching and steering . . . 34
  - 4.1.1 Matching interface . . . 36
  - 4.1.2 Steering interface . . . 37

4.1.3 Regular use for beam transport 38
4.2 PETS measurements screen 38
4.2.1 BPM pulse display 39
4.2.2 Beam steering in the PETS 40
4.2.3 Power production display 40

5 PETS Power production experiments 42
5.1 Measurements and predictions 42
5.1.1 Form factor estimations 42
5.1.2 Power production used for machine conditioning 44
5.2 Correlations of power and beam position 45
5.2.1 Power in the two PETS arms 46
5.2.2 Changes in phase 47
5.2.3 The effect of the beam position and future work 48

6 Conclusion and outlooks 50

Bibliography 51

List of Figures 54

A List of abbreviations i

B Calibration of the PETS IQ demodulator ii

C Collection of publications vii

D Extra figures xiv

Chapter 1

Introduction

This M.Sc. thesis concerns accelerator research related to the CLIC Test Facility 3, which is an experimental facility used to demonstrate key concepts of the Compact Linear Collider (CLIC) scheme. CLIC is an international study of a future multi-TeV electron-positron collider.

Specifically, the thesis describes power production experiments in Power Extraction and Transfer Structures, which lies at the heart of the CLIC scheme. In addition, the development of a graphical user interface (GUI) in Matlab is documented. The GUI is used in the control room of the test facility for monitoring and experiments.

The introduction describes present-day CERN, and the motivation for a new high-energy particle collider. An outline of the thesis is provided at the end of the chapter.

1.1 About CERN

CERN (originally *Conseil Européen pour la Recherche Nucléaire*) is the European laboratory for particle physics, and one of the world's largest centres for scientific research [1]. The organization was founded in 1954, partly to revive and reunite European science after the second world war. CERN has at present 20 member states, Norway included. Approximately 2,500 people are employed full-time, while 8,000 scientists from 580 universities and 85 nationalities visit CERN for their work. The laboratory is situated on the Franco-Swiss border near the city of Geneva. Since the start, 3 Nobel prizes in physics have been awarded to people affiliated with CERN.

The main activities at the laboratory today is high-energy physics, which is mainly concerned with the study of interactions between particles. This type of basic research provides knowledge of the universe, ranging from the building blocks of what all matter is made of, the basic forces that interact between them and eventually an understanding of other types of matter than we are used to in our daily life (like dark matter and dark energy). Most of this research is done by studying high-energy collisions between particles, as the interacting particles are annihilated and produce showers of other particles. The exchange of mass and energy is a result of Einstein's famous equation $E = mc^2$. Before the collisions, beams of particles are accelerated to approximately the speed of

light in vacuum, and the collisions are observed with huge particle detectors.

CERN has received much attention the last years because of its newest collider, which is called the Large Hadron Collider (LHC). This is the world's largest particle accelerator, a ring 27 km in circumference and situated about 100 meters below ground [1]. The LHC is installed in the same tunnel as the former Large Electron-Positron (LEP) accelerator, and is used to collide two beams of protons or two beams of heavy ions. Starting in March 2010, the LHC collided two 3.5 TeV beams of protons for a total collision energy of 7 TeV (when two beams of the same energy are collided, the collision energy is the sum of the two). 3.5 TeV is the energy a particle of unit charge – like a proton or electron – gets after being accelerated through an electric field of $3.5 \cdot 10^{12}$ V. This is already 3.5 times higher than the previous highest energy, at the Tevatron at Fermilab. Still, the schedule is to ramp up the energy to 14 TeV at the interaction point in the coming years.

The amount of data generated by the LHC is enormous, and it will produce roughly 15 petabytes (15 million gigabytes) of data anually. Before the data is stored, a large fraction of collision data is filtered out, since only the most interesting collisions from a physics point of view are recorded in the detectors. Still, a vast amount of data remains to analyze, so a special computing infrastructure called *the Worldwide LHC Computing Grid* is used to handle it. This system distributes the data to computing centres all over the world, where computing resources are available. Information technology is, and has for a long time been, a large part of CERN; one of the biggest achievements was the development of the World Wide Web in 1989.

1.2 Looking towards the future

The LHC has started operation, but accelerator scientists are not resting on their laurels. In fact, there have been studies going on for many years concerning the next collider for high-energy physics. LHC, being a *hadron collider*, is a 'discovery' machine where new particles are expected to be found. There is also another possible type of collider, which collides *leptons* like electrons. Traditionally, hadron and lepton colliders have been alternating, because lepton colliders can study the phenomena discovered in hadron colliders in more detail. Thus, the consensus is that the next collider should be a lepton collider.

There are basically two shapes that are used in particle accelerators – rings and straight lines. The main part of the LHC is a ring, and the main benefit of using a ring is that the particles can circulate many times, while gaining energy in each circulation before they eventually collide. However, when particles are bent around a ring, they emit *synchrotron radiation* [2], which is proportional to $P_S \propto \frac{1}{m_0^4}\frac{E^4}{R^2}$, where m_0 is the rest mass of the particle, E is the particle energy and R is the bending radius of the particle orbit. The synchrotron radiation causes particles to lose energy, and must therefore be kept within reasonable limits. By looking at the equation, we see that the particle energy has a much larger impact on the synchrotron radiation than the radius. Since future experiments will require higher collision energies than in earlier lepton colliders, we can rule out ring colliders because of the immense size that would

be required[1]. The rest mass of the proton is ca. 1836 times higher than the rest mass of the electron, so we can also see from the equation that synchrotron radiation has the largest impact on electron colliders.

There are two large international studies for the next high-energy collider, which because of the reasons above should be a linear lepton collider. One of them is the International Linear Collider (ILC) [3], with a designed collision energy of 0.5 TeV (with a possible upgrade to 1 TeV) and an estimated length of 31 km, in addition to two *damping rings* of 6.7 km circumference. In order to keep the length as short as possible, one needs a high electric field for acceleration. This so-called *gradient* is 31.5 Megavolts per meter, which is to be achieved with superconducting *RF cavities* made of niobium, operating at a temperature of 2 K.

The second large study is called the Compact Linear Collider (CLIC) [4], which this thesis is a part of. CLIC is designed with a collision energy of 3 TeV and a length of 48.4 km [5]. CLIC therefore aims for a 6 times higher energy than the ILC, for a ca. 50 % longer machine. A more detailed treatment of the pros and cons of the two accelerator schemes is given in [6]. To achieve the design gradient of 100 MV/m, a novel accelerator concept has been developed which utilizes two beams in each direction. One of the beams is called the *drive beam* and is decelerated in specially designed *Power Extraction and Transfer Structures* (PETS), described in Chapter 2.7. The power produced in the PETS is transferred to the main beam for acceleration.

CLIC is currently a feasibility study, which means that the technology must be proved. As part of this, a prototype accelerator called the *CLIC Test Facility 3* (CTF3) is housed at CERN as part of an international collaboration. The facility contains two main experiments, which are the Two-Beam Test Stand (TBTS) and the Test Beam Line (TBL) [7]. This thesis describes work and experiments with the TBL.

When the LHC starts to provide results with indications of new physics, a choice of the next collider can be taken based on the collision energy and the desired technology.

1.3 Outline of the thesis

Chapter 2 explains the theory of accelerator physics which this thesis is based upon. The relevant topics are explained starting with the basics of how the electromagnetic force affects a charged particle, before moving on to more advanced topics like wakefields and beam diagnostics. The last section of the chapter is devoted to Power Extraction and Transfer Structures (PETS), which is a core technology of the CLIC scheme.

Chapter 3 describes the first prototype for the CLIC decelerator, namely the Test Beam Line (TBL). First, the nominal parameters are described, as well as the current status. Second, the method of the PETS power measurements is explained.

In Chapter 4, a description is given of the TBL Graphical User Interface which was developed for commissioning and experiments with the TBL. The

[1] As an example, a radius approximately 25 times larger than the LHC would be needed to go from the LEP accelerator's final energy of 0.1045 TeV to 0.5 TeV per beam.

functionality of the different parts of the program is explained, as well as a short description of the normal use.

The main results of the power production experiments with the PETS in the TBL are given in Chapter 5. First, basic power production measurements are described, and how these are used for conditioning the rest of the CTF3 machine. The rest of the chapter describes experimental data of how the beam position inside the PETS affects the power production.

1.4 Acknowledgements

There are many people who have helped me during my year at CERN. First and foremost, I want to thank my supervisors Steffen Döbert (CERN), Erik Adli (CERN and the University of Oslo) and Lars Lundheim (The Norwegian University of Science and Technology) for excellent scientific guidance and for always leading me on the right path. In addition, I want to thank Roberto Corsini, Frank Tecker and the rest of the CTF3 team, Steve Smith and Erk Jensen for valuable advice and explanations[2].

Steinar Stapnes and the University of Oslo provided funds for a USPAS (United States Particle Accelerator School) course in the beginning of the year, which allowed me to learn essential theory for the project.

Finally, I also want to thank my closest family for their continuing support, and Egil and Danielle for providing the inspiration to start at CERN in the first place and for the stay in the beginning of the year (as well as many good dinners!).

[2]Frank Tecker also for rigorously hunting down and killing my Matlab processes!

Chapter 2

Accelerator physics

This thesis is written on a foundation of accelerator physics, and this chapter aims to explain the topic to people not working in the field. First, the basic principles of guiding single particles and a whole beam is explained in Section 2.1. Section 2.2 describes wakefields – which originates from the electromagnetic interaction between the particle beam and the beam pipe, and which is the main mechanism behind power production in the CLIC scheme. Section 2.3 describes radiofrequency (rf) systems used for efficient acceleration of particles, both with standing and travelling waves. Section 2.5 explains how measurements are done on a particle beam, and Section 2.6 describes how one can steer a beam through an accelerator. Finally, Section 2.7 details the *Power Extraction and Transfer Structure* (PETS), which is used in the CLIC scheme to transfer energy from one beam to another.

2.1 Dynamics of charged particle beams

Beam dynamics is the understanding of the motion of a beam of charged particles controlled by external electromagnetic fields through an accelerator. This section explains how a beam is moving through a combination of magnets in an accelerator, how the motion can be calculated easily and also describes important parameters of the beam. The ideas presented here are well established in accelerator physics, and are taken mostly from [2].

2.1.1 Basic principles

To do work on any object, one needs a force. There are four fundamental forces in nature, being gravitation, electromagnetism, and the strong and weak interactions. The strong force only works between particles with a net color charge, i.e., quarks and gluons, and holds *hadrons* (particles composed of quarks) and nuclei together. Of the remaining three forces, electromagnetism is around 10^{11} times stronger than the weak force and 10^{40} times stronger than gravity[1], when forces are compared between particles interacting in more than one way [8]. Thus, the electromagnetic force is the one that must be considered for work on

[1] The indicated strength ratios depend on the nature of the source and the distance. They are therefore not meant to be absolute, but to reflect that there is a large difference.

charged particles like electrons and protons, since the strong and weak forces are short-ranged and both the weak interaction and gravity are negligible.

A particle of elementary charge in an electromagnetic field experiences the Lorentz force

$$\vec{F} = e(\vec{E} + \vec{v} \times \vec{B}), \tag{2.1}$$

where $e = 1.602 \times 10^{-19}$ C is the elementary charge, $\vec{E}$ is the electrical field, $\vec{v}$ is the particle velocity and $\vec{B}$ is the magnetic field. The work done by the Lorentz force on the particle over a path C is then given by the work integral

$$W = \int_C \vec{F} \cdot d\vec{l} = e \int_C \vec{E} \cdot d\vec{l} + e \int_C \left(\vec{v} \times \vec{B}\right) \cdot d\vec{l}. \tag{2.2}$$

Looking at the second term on the right side, we see that the cross product is perpendicular to both $\vec{v}$ and $\vec{B}$. Since the path element $d\vec{l}$ is parallel to the velocity vector $\vec{v}$, the dot product is therefore zero. This leads to the important result that magnetic fields cannot do work on and change the energy of a particle, they can only change the trajectory. The electric field is therefore responsible for accelerating the particle. A more detailed treatment of how electric fields are used for acceleration is given in Section 2.3.

To guide a beam of particles on a defined trajectory, with forces perpendicular to the particle's direction of motion, one might use both the electric and magnetic fields. However, by looking at (2.1), we see that the two fields would act with the same force on the particle if $|\vec{E}| = v|\vec{B}|$. Since the particles are accelerated to approximately the speed of light in vacuum[2], we have $|\vec{E}| \approx c|\vec{B}|$. That is, a magnetic field of $B = 1$ T is equivalent to an electric field strength of $E = 3 \times 10^8$ V/m. It is relatively easy to produce a magnetic field of 1 T, but certainly not an electric field of $E = 3 \times 10^8$ V/m (particularly because of electrical breakdowns). Therefore, magnets are almost always used to steer beams in accelerators at high energies.

The conventional coordinate system used in beam dynamics is a *curvilinear* Cartesian coordinate system $K = (x, y, s)$ that moves along the ideal trajectory of the beam. That is, the s coordinate is moving along the ideal trajectory, the x coordinate is perpendicular in the horizontal direction and the y coordinate is perpendicular in the vertical direction. The direction along s is called *longitudinal*, while the x and y directions are called *transverse*. The coordinate z can also be used for the longitudinal direction, and represents relative distances.

The ideal trajectory of the beam is enclosed in a metallic pipe which is known as the *beam pipe*. One reason for this is because the beam needs to be transported smoothly without interacting with particles in the air. It is therefore a vacuum inside, and the pipe is thus also known as the *vacuum chamber*.

2.1.2 Magnet types

There is a variety of magnet shapes and types in use in accelerators, but most of them can be characterized by the number of poles. The *dipole* and the

[2] As an example, the LHC at its full energy has a Lorentz factor of $\gamma = \sqrt{\frac{1}{1-(v/c)^2}} = \frac{E}{m_0 c^2} = 7461$, for an energy of $E = 7$ TeV per beam and a proton rest mass of $m_0 = 938$ MeV/c^2. This corresponds to a velocity of $v = 0.999999991c$.

quadrupole make up linear systems and will be described here, but there are also more types like sextupoles, octupoles and others.

The magnetic field B_y in one plane in the vicinity of the particle trajectory, multiplied by the elementary charge e and divided by a particle momentum p, may be expanded by a Taylor series as [2]

$$\begin{aligned}\frac{e}{p}B_y(x) &= \frac{e}{p}B_{y0} + \frac{e}{p}\frac{dB_y}{dx}x + \frac{e}{p}\frac{1}{2!}\frac{d^2B_y}{dx^2}x^2 + \frac{e}{p}\frac{1}{3!}\frac{d^3B_y}{dx^3}x^3 + \dots \\ &= \frac{1}{R} + kx + \frac{1}{2!}mx^2 + \frac{1}{3!}ox^3 + \dots\end{aligned} \tag{2.3}$$

where the first term on the right side is the dipole term with *bending radius* R, the second is the quadrupole term with *focusing strength* k, the third is the sextupole term with strength m, the fourth is the octupole term with strength o and so on. The y component of the field is shown here, but the x component follows a similar pattern (with a dependance on the y position).

A dipole consists of two parallell poles and is used for changing the trajectory of the beam. The definition of the dipole effect is therefore $\frac{e}{p}B_y = \frac{1}{R}$, where R is the *bending radius* of the magnet. Thus, a larger magnetic field corresponds to a smaller bending radius, which means that the trajectory is bent more. It is important to note that ideal dipoles usually only bend in one transverse plane, while the behaviour in the other plane is like that of empty space, which is known as a *drift space*. Dipoles are normally placed with the poles above and below the particle trajectory, so that the trajectory is bent in the horizontal plane.

A quadrupole consists of four symmetrical poles around the particle trajectory, and is used for focusing or defocusing the beam. Quadrupoles are needed since the particles will spread out over time because of effects like the Coulomb interaction. In a focusing quadrupole, a particle far from the ideal trajectory would be more deflected towards the centre than a particle close to the ideal trajectory. All particles are focused into a *focal point*, in the same way as for a lens in paraxial, geometric light optics (the optics analogy is often used in accelerator physics). Only including the quadrupole term in (2.3), the equation for a quadrupole is $\frac{e}{p}B_y(x) = kx$, where k is the energy independent *focusing strength* of the magnet. Quadrupole magnets have the property that they will focus a particle beam in one transverse plane, but defocus it in the other transverse plane. By convention the term *focusing magnet* usually means focusing in the horizontal plane, while *defocusing magnet* usually means defocusing in the horizontal plane. However, it is still possible to achieve a net focusing in both planes; one possibility is by combining a focusing and a defocusing magnet with a drift space in between. This combination is called a *FODO cell* (the name is an abbreviation for focusing and defocusing magnets with non-focusing elements like empty space or dipoles in between) [9].

Real magnets will generally include more than one term, one example is the *weak focusing* effect of a dipole. However, clever magnet design can minimize the effects of unwanted terms [9]. The combination of pure dipole and quadrupole magnets is called *linear optics*.

2.1.3 Particle trajectories and transfer matrices

If the bending of particle trajectories is restricted to the horizontal x plane, and we use linear beam dynamics, we have the following magnetic fields present:

$$\frac{e}{p}B_x = -ky,$$
$$\frac{e}{p}B_y = B_{y0} + kx,$$

where B_{y0} is the dipole field and k is the focusing strength of the magnet. Under these conditions, and assuming particles with ideal energy, we may derive the equations of motion of the curvilinear system [9]:

$$x'' + \left(k_0 + \kappa_{0x}^2\right) x = 0, \tag{2.5a}$$
$$y'' - k_0 y = 0. \tag{2.5b}$$

The derivatives are taken with respect to the longitudinal coordinate s. Here κ_0^2 is the bending curvature of the ideal path and k_0 is the ideal focusing strength. If we set $K = (k_0 + \kappa_{0x}^2)$ in the horizontal plane and $K = -k_0$ in the vertical plane, the principal solutions to such a system for $K > 0$ is

$$C(s) = \cos\sqrt{K}s \qquad \text{and} \qquad S(s) = \frac{1}{\sqrt{K}}\sin\sqrt{K}s. \tag{2.6}$$

For $K < 0$ we get the solutions

$$C(s) = \cosh\sqrt{|K|}s \qquad \text{and} \qquad S(s) = \frac{1}{\sqrt{|K|}}\sinh\sqrt{|K|}s. \tag{2.7}$$

An arbitraty solution can then be expressed as a linear combination of the two principal solutions:

$$u(s) = C_u(s)u_0 + S_u(s)u_0', \tag{2.8a}$$
$$u'(s) = C_u'(s)u_0 + S_u'(s)u_0', \tag{2.8b}$$

where u may represent either x or y, the derivatives are taken with respect to s and u_0 and u_0' are initial conditions of the particle trajectory. This solution may be written more elegantly in matrix notation:

$$\begin{pmatrix} u(s) \\ u'(s) \end{pmatrix} = \begin{pmatrix} C_u(s) & S_u(s) \\ C_u'(s) & S_u'(s) \end{pmatrix} \begin{pmatrix} u_0 \\ u_0' \end{pmatrix}. \tag{2.9}$$

We will here show two types of matrix equations in common use. One is for a *drift space*, where there are no specific elements except for the vacuum chamber. Here the focusing parameter $K = 0$ and by using (2.6) or (2.7) together with (2.9) we get

$$\begin{pmatrix} u(s) \\ u'(s) \end{pmatrix} = \begin{pmatrix} 1 & l \\ 0 & 1 \end{pmatrix} \begin{pmatrix} u_0 \\ u_0' \end{pmatrix}. \tag{2.10}$$

Here the parameter l is the length of the drift space. As can be seen from this equation, the final position is the same as the initial position in addition to the change from the slope over the distance l, while the slope remains the same.

An ideal quadrupole has $K = k \neq 0$, so the solution for a quadrupole of length l and focusing strength $k > 0$ is

$$\begin{pmatrix} u(s) \\ u'(s) \end{pmatrix} = \begin{pmatrix} \cos\sqrt{k}l & \frac{1}{\sqrt{k}}\sin\sqrt{k}l \\ -\sqrt{k}\sin\sqrt{k}l & \cos\sqrt{k}l \end{pmatrix} \begin{pmatrix} u_0 \\ u_0' \end{pmatrix}. \tag{2.11}$$

For $k < 0$ the solution is

$$\begin{pmatrix} u(s) \\ u'(s) \end{pmatrix} = \begin{pmatrix} \cosh\sqrt{|k|}l & \frac{1}{\sqrt{|k|}}\sinh\sqrt{|k|}l \\ \sqrt{|k|}\sinh\sqrt{|k|}l & \cosh\sqrt{|k|}l \end{pmatrix} \begin{pmatrix} u_0 \\ u_0' \end{pmatrix}. \tag{2.12}$$

Solutions in matrix form are used a lot, and the matrices are called *transfer matrices* since they describe the transfer functions from one point to another. Each of the equations (2.8) to (2.12) contains one transfer matrix $\mathcal{M}$ that describes the motion of one particle from one point to another. The elegancy of using transfer matrices is that many single elements $\mathcal{M}_i$ may be combined into one total transfer matrix $\mathcal{M}$ by multiplication:

$$\mathcal{M} = \mathcal{M}_N\mathcal{M}_{N-1}\cdots\mathcal{M}_3\mathcal{M}_2\mathcal{M}_1. \tag{2.13}$$

The combination of different elements, including magnets and drift spaces, is called a *lattice*. With the matrix formalism one may calculate the particle motion through an arbitrary lattice, as long as one knows the lengths and magnetic strengths of the elements. The separation into uniform pieces is called the *hard edge model* since it does not take into account the fringe fields in the magnets. This approximation is valid for most practical purposes [9].

2.1.4 Phase space, emittance and the Twiss parameters

The trajectory of a single particle through an arbitrary lattice can be calculated using transfer matrices as described in the previous section. However, to understand the motion of a whole beam of particles this is not so convenient [2]. Instead, we may solve the equation of motion analytically and get a closed-form solution. The differential equation of motion is

$$u'' + K(s)u = 0, \tag{2.14}$$

where u can be either x or y, and $K(s)$ is an arbitrary distribution of focusing along the beam line. For a general solution we may use an ansatz with an s-dependent amplitude and phase:

$$u(s) = \sqrt{\varepsilon}\sqrt{\beta(s)}\cos\left[\psi(s) - \psi_0\right]. \tag{2.15}$$

By using this function with the constraint that the phase $\psi(s)$ must be valid everywhere, we arrive at a constant of motion [9]

$$\gamma(s)u^2(s) + 2\alpha(s)u(s)u'(s) + \beta(s)u'^2(s) = \varepsilon, \tag{2.16}$$

where $\alpha = -\frac{1}{2}\beta'$ and $\gamma = (1+\alpha^2)/\beta$. This is the equation of an ellipse, which is shown in Figure 2.1. The area of the ellipse is constantly $\pi\varepsilon$, where ε is called the *emittance* and represents the distribution of particles in one phase space plane. The defined ellipse depends on the particle distribution, and the particles inside

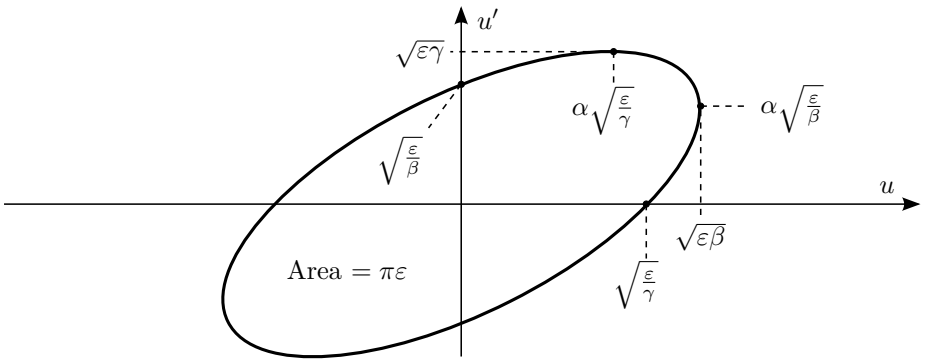

Figure 2.1: The phase space ellipse in the (u, u') plane

will stay inside. The fact that the emittance does not change with a linear lattice is a result of *Liouville's theorem*, which states that under the influence of conservative forces the particle density in phase space is constant [9, 10]. The other defining parameters α, β, γ will however change along the beam trajectory, so the ellipse will change its shape. One example is in a drift space, where the ellipse will expand horizontally while the vertical distribution stays the same (since the particle angles do not change).

The particles in the beam follow trajectories defined by (2.15). By selecting those particles for which the cosine term is ± 1, we get the *envelope* of the beam. For a beam with a Gaussian particle distribution, this envelope contains one standard deviation of the particles,

$$\sigma(s) = \pm\sqrt{\varepsilon}\sqrt{\beta(s)}. \tag{2.17}$$

The particles will move inside this envelope with the same period, and this is called *betatron motion*. The transverse *beta functions* $\beta(s)$ change along the lattice because of focusing, defocusing and drift spaces. The three parameters α, β, γ are known as the *Twiss parameters*.

The Twiss parameters can be transported in the same way as individual particles, by using transfer matrices as described in Section 2.1.3. If we define the *beam matrix*

$$\mathbf{\Sigma}_0 \equiv \varepsilon \begin{pmatrix} \beta_0 & -\alpha_0 \\ -\alpha_0 & \gamma_0 \end{pmatrix} \tag{2.18}$$

at one position, and $\mathcal{M}$ is the transfer matrix for an arbitrary lattice, it can be shown [2] that the beam matrix (with Twiss parameters) at the new position is

$$\mathbf{\Sigma}_1 = \mathcal{M}\, \mathbf{\Sigma}_0\, \mathcal{M}^{\mathrm{T}}. \tag{2.19}$$

The emittance in (2.16) is no longer constant when the particle beam is accelerated or decelerated. Liouville's theorem states that a phase space element $\Delta u \Delta p_u$ remains constant, where $\Delta p_u = p_0 u'$ and p_0 is the particle momentum. When the momentum increases, the corresponding element $\Delta u \Delta u'$ in Figure 2.1 must be reduced to keep the product $\Delta u \Delta p_u$ constant. This reduction of the emittance with acceleration is called *adiabatic damping*. Correspondingly, the increase in emittance with deceleration is called *adiabatic undamping*. The emittance ε defined so far is called the *geometric emittance*. A parameter which is

kept constant even when accelerated or decelerated is the *normalised emittance* defined by

$$\varepsilon_N = \beta\gamma\varepsilon, \tag{2.20}$$

where $\beta = v/c$ and $\gamma = 1/\sqrt{1-\beta^2}$, neither of which must be confused with the Twiss parameters.

The emittance is often considered for a particular plane of interest, i.e., the horizontal, vertical or longitudinal emittance. Each of these has a two-dimensional distribution, and the total phase space therefore has six dimensions.

2.1.5 Matching of beam optics

For a defined lattice with given magnet strengths, the Twiss parameters can be transported to an arbitrary position by using (2.19). However, in many cases the problem is the opposite; specific parameter values are desired at a chosen position, and the solution lies in varying the magnet strengths. This procedure is called *matching of beam optics*. The functions that can be optimized are the Twiss parameters α, β, γ in the vertical and horizontal plane, and the dispersion of the particle beam. It is usually desired to optimize several of these functions at once, at one point in the lattice. We will therefore derive a method for optimizing an arbitrary number of functions, based on [2].

We choose n arbitrary functions $f_1, f_2, \ldots, f_i, \ldots, f_n$ for matching. To adjust these values we have $m \geq n$ quadrupoles available with magnet strengths $k_1, k_2, \ldots, k_j, \ldots, k_m$, but in the calculation we choose $m = n$. Each of the n functions depends on the strengths of all n quadrupoles as $f_i = f_i(k_1, k_2, \ldots, k_n)$. First we use some initial values $k_{10}, k_{20}, \ldots, k_{n0}$ for the magnet strengths. The corresponding functions are then $f_{10}, f_{20}, \ldots, f_{n0}$, while the ideal functions are $f_{1d}, f_{2d}, \ldots, f_{nd}$.

The difference between the first ideal function f_{1d} and the current value f_{10} can be expanded as

$$\begin{aligned} f_{1d} - f_{10} =& \frac{\partial f_1}{\partial k_1}(k_1 - k_{10}) + \frac{1}{2}\frac{\partial^2 f_1}{\partial k_1^2}(k_1 - k_{10})^2 + \ldots \\ &+ \frac{\partial f_1}{\partial k_2}(k_2 - k_{20}) + \frac{1}{2}\frac{\partial^2 f_1}{\partial k_2^2}(k_2 - k_{20})^2 + \ldots \\ &\vdots \\ &+ \frac{\partial f_1}{\partial k_n}(k_n - k_{n0}) + \frac{1}{2}\frac{\partial^2 f_1}{\partial k_n^2}(k_n - k_{n0})^2 + \ldots \end{aligned} \tag{2.21}$$

This is an infinite series in several variables, and cannot be used in practice. Instead, we may linearize it and neglect all quadratic and higher-order terms. Including all functions, we then have

$$\begin{aligned} f_{1d} - f_{10} &= \frac{\partial f_1}{\partial k_1}(k_1 - k_{10}) + \frac{\partial f_1}{\partial k_2}(k_2 - k_{20}) + \cdots + \frac{\partial f_1}{\partial k_n}(k_n - k_{n0}), \\ f_{2d} - f_{20} &= \frac{\partial f_2}{\partial k_1}(k_1 - k_{10}) + \frac{\partial f_2}{\partial k_2}(k_2 - k_{20}) + \cdots + \frac{\partial f_2}{\partial k_n}(k_n - k_{n0}), \\ &\vdots \\ f_{nd} - f_{n0} &= \frac{\partial f_n}{\partial k_1}(k_1 - k_{10}) + \frac{\partial f_n}{\partial k_2}(k_2 - k_{20}) + \cdots + \frac{\partial f_n}{\partial k_n}(k_n - k_{n0}). \end{aligned} \tag{2.22}$$

This can be written in matrix notation as

$$\begin{pmatrix} f_{1d} \\ f_{2d} \\ \vdots \\ f_{nd} \end{pmatrix} - \begin{pmatrix} f_{10} \\ f_{20} \\ \vdots \\ f_{n0} \end{pmatrix} = \begin{pmatrix} \frac{\partial f_1}{\partial k_1} & \frac{\partial f_1}{\partial k_2} & \cdots & \frac{\partial f_1}{\partial k_n} \\ \frac{\partial f_2}{\partial k_1} & \frac{\partial f_2}{\partial k_2} & \cdots & \frac{\partial f_2}{\partial k_n} \\ \vdots & \vdots & \ddots & \vdots \\ \frac{\partial f_n}{\partial k_1} & \frac{\partial f_n}{\partial k_2} & \cdots & \frac{\partial f_n}{\partial k_n} \end{pmatrix} \left[\begin{pmatrix} k_1 \\ k_2 \\ \vdots \\ k_n \end{pmatrix} - \begin{pmatrix} k_{10} \\ k_{20} \\ \vdots \\ k_{n0} \end{pmatrix} \right]. \tag{2.23}$$

The matrix that contains the elements $\partial f_i/\partial k_j$ shows how much each function depends on each quadrupole strength, and is known as the *response matrix* $\mathbf{R}$. Equation (2.23) can be written

$$\mathbf{F}_d - \mathbf{F}_0 = \mathbf{R}(\mathbf{K} - \mathbf{K}_0). \tag{2.24}$$

Solving this for $\mathbf{K}$, we will in general find better values for the quadrupole strengths. The improved values may then be inserted back into the equation in place of $\mathbf{K}_0$, and the process may be repeated to give even better values[3]. The equation for one iteration is then

$$\mathbf{K}_{p+1} = \mathbf{K}_p + \mathbf{R}_p^{-1}(\mathbf{F}_d - \mathbf{F}_p). \tag{2.25}$$

where the index p indicates the iteration number. Each element of the response matrix $\mathbf{R}$ may be calculated numerically as

$$\frac{\partial f_i}{\partial k_j} = \frac{f_i(k_1, k_2, \ldots, k_j + \Delta k, \ldots, k_n) - f_i(k_1, k_2, \ldots, k_j, \ldots, k_n)}{\Delta k}. \tag{2.26}$$

The whole calculation of (2.25) is time consuming to do by hand, but relatively fast on a computer. Therefore it is common to use computer programs, one example being MAD [11].

2.2 Wakefields

A stationary charged particle will have an electric field associated with it. For a pointlike positive particle in free space, the field lines will go directly outwards, as shown to the left in Figure 2.2. When the particle obtains a relativistic velocity, the field lines will get Lorentz contracted when observed from the stationary laboratory frame. The angular spread is on the order of $\frac{1}{\gamma}$, where γ is the Lorentz energy factor. This field distribution is shown in the middle of the figure. For a particle traveling with the speed of light, the field would resemble an infinitely thin disk travelling with the particle.

A particle travelling through a cylindrical beam pipe of a perfectly conducting material will have the same behaviour, if travelling along the axis [12]. In this case, the field lines would simply be truncated at the pipe wall. If the particle had a certain offset with respect to the axis of the beam pipe, or if the beam pipe was not cylindrical, then the fields would be perturbed from the free space values. However, as long as the beam pipe is perfectly conducting, neither the

[3]Sometimes the iterations will not converge to a useful solution. The iterative process can for instance get stuck in a local minimum and oscillate around it, or it may not give a physically meaningful solution (The beam size may become too big for the aperture of the beam pipe, or the quadrupole strengths may not be achievable).

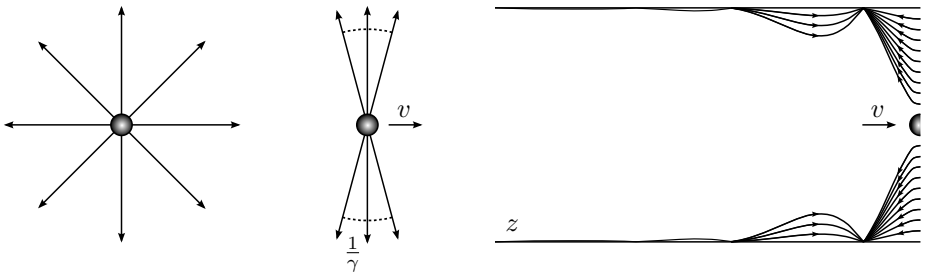

Figure 2.2: Left: A charged particle in free space. Middle: A charged particle with a relativistic velocity. Right: Monopole wakefield left after a charged particle travelling through a resistive beam pipe.

particle itself nor other particles in the beam pipe would experience any effect. For any type of beam pipe, there are image currents on the pipe wall travelling with the particle. In the perfectly conducting case, this current would travel unhindered.

The situation is different when the pipe wall is not perfectly conducting, as is the case for a normal beam pipe. The beam and the image current then experience an impedance, which leads to a longitudinal electric field component. The field is no longer restricted to a thin disk, but there will be a field trailing the particle. The particle is assumed to travel with a velocity close to the speed of light, so because of causality there cannot be a field ahead of the particle, only behind it. This is the origin of the name *wake field*, since the particle leaves a field behind it in the same way a ship leaves a wake in the water.

Another cause of wake fields is when the cross section changes along the beam pipe. This is especially important for standing wave cavities and travelling wave structures, as described in Section 2.3. When designing such structures, one must also account for the effects of wake fields. Since the fields are generally quite complicated, numerical codes are normally used in the calculation.

The wake field can have both longitudinal and transverse components. Particles travelling behind the leading particle will experience a force according to their relative positions. The longitudinal wake field component can thus either accelerate or decelerate the trailing particles, while the transverse field components can deflect the particles transversally.

A beam of particles can be decomposed in different multipole moments. Each multipole moment will induce a wake potential of the same order [12]. The wake potentials are therefore called monopole wake, dipole wake, and so on. The *monopole* wake is usually dominant for longitudinal effects on the beam [12]. The longitudinal field distribution for this moment is shown to the right in Figure 2.2, for the case of a resistive wall. A particularity of the monopole wake is that the longitudinal field component only depends on the longitudinal position, and is constant transversally. The *dipole* wake is usually dominant for transverse effects, which can be harmful to the beam.

As seen from the field lines in Figure 2.2, the field close to the leading particle will act to decelerate it. The particle will therefore lose energy because of its electromagnetic interaction with the beam pipe. This energy loss in eV is equal to half of the electric field in V immediately behind the particle, so the particle only sees half of the field it produces [12].

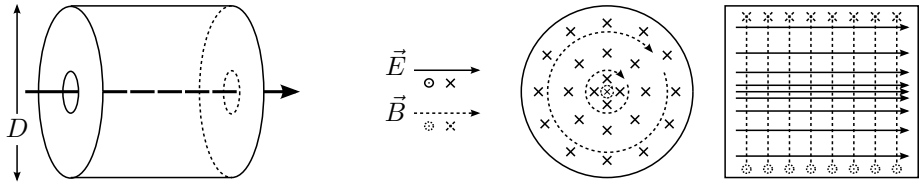

Figure 2.3: A cylindrical pillbox cavity. The basic structure is shown on the left, with diameter D. The transversal electric and magnetic fields for the TM_{010} mode are shown in the middle, while the longitudinal fields for the same mode are shown on the right.

2.3 RF systems for particle acceleration

The simplest way to accelerate charged particles is to use an electrostatic field. This concept was used in the first particle accelerators and in daily life applications like analog *cathode ray tube* (CRT) TVs. The principle is to have a static electric field inside a vacuum tube, and a particle source in one end. The particles will then be accelerated by the electric field and collected in the other end of the tube. The particles will increase in energy while they travel, but are limited by the magnitude of the electric field. Typically, particles of unit charge (like electrons or protons) can reach an energy of a few MeV before effects like electric breakdown occur. The effective electric field used for acceleration per unit length is called the *gradient*.

To achieve higher energies than this, numerous designs have been used in the past, but a common scheme in particle accelerators today is to have a series of resonant, standing wave cavities. The cavities will accelerate the particles step by step along the way. This is done by using alternating electric fields oscillating at radio frequencies, as described in Section 2.3.1. Another scheme that is used in modern linear accelerators is to use loaded waveguides with travelling waves, and this explained in Section 2.3.2.

2.3.1 Resonant standing wave cavities

A cavity can be any hollow container with conducting walls, which allows an electrical field to exist inside. Generally, the preferred shape in particle accelerators is cylindrical, for symmetry reasons around the beam. A cavity is a resonator, and allows standing waves for certain frequencies depending on the size.

A simple example of a cavity is the pillbox cavity shown in Figure 2.3. There is an infinite number of *modes* that can exist in this cavity, but TEM- and TE-modes are not of interest for acceleration since they do not have an electric field component in the longitudinal direction, and therefore do not accelerate the beam in the direction of propagation. Of the TM modes, the TM_{010} has the lowest resonance frequency [13] and is usually considered the most interesting. The field lines of this mode are shown to the right in Figure 2.3.

If a negatively charged particle (like an electron) enters the cavity and sees a positive field, it will be attracted to it and accelerated, but if it sees a negative field, it will instead be decelerated. Thus, to continuously accelerate particles

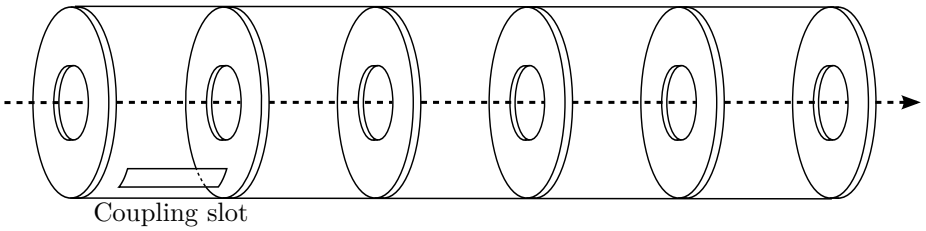

Figure 2.4: A basic travelling wave structure with iris-shaped screens.

one may use a series of cavities synchronized so that the particles always see an attractive field ahead when they enter a new cavity.

The fields can be arranged to allow acceleration of particles at certain positions and times, but particles that see the opposite phase will be decelerated. Therefore, particles cannot be sent in a continuous beam. Instead, billions of particles are combined into *bunches* which have a certain spacing in between[4].

A particle beam can excite different modes in a cavity. Other modes than the fundamental mode make the effects on the beam more complicated, and these so-called *higher order modes* (HOMs) are generally not wanted. By making more sophisticated structures than the simple pillbox cavity, it is possible to introduce *damping* of higher order modes.

2.3.2 Travelling wave accelerating structures

In linear accelerators, one may also use waveguide-like structures for acceleration. However, normal waveguides will not accelerate the beam since the phase velocity is greater than the speed of light [2]. The particles, which are moving more slowly (since they cannot travel faster than the speed of light), would therefore be accelerated in half of the wave period and decelerated in the other half of the period.

A phase velocity below the speed of light is achieved by inserting iris-shaped screens [2], as shown in Figure 2.4. The whole structures can be used with either standing waves or travelling waves. The choice is made by either using a reflection-free boundary at the end and thereby absorbing the wave, or by using a near-lossless boundary which causes standing waves.

The irises form a periodic structure within the waveguide, reflecting waves as they pass through and causing interference. Wave propagation can only occur when the wavelength λ is an integer multiple of the iris separation d,

$$\lambda = nd, \qquad n = 1, 2, 3, \ldots. \tag{2.27}$$

Therefore the irises only allow certain wavelengths to travel in the waveguide. There are three modes that are used in practice for linear accelerators, corresponding to $n = 2, 3$ or 4, with $n = 3$ being the dominant [2]. In other words, the irises are spaced at a certain *phase advance* of the wavelength, and the three choices mentioned are called the π mode, the $2\pi/3$ mode and the $\pi/2$ mode, respectively.

[4] As an example, at nominal operation the LHC will have 1.15×10^{11} protons in each bunch at the start, 2808 bunches per beam in the main ring and a minimum of 7 meters between each bunch [14].

We will now define some important parameters used for travelling wave structures. If E is the travelling wave longitudinal electric field for a propagating wave with power flow P, the shunt impedance per unit length is [15]

$$R' = \frac{E^2}{|dP/ds|}. \tag{2.28}$$

The shunt impedance describes the effective acceleration per input power. Quantities per unit length will in general be denoted with a prime ('). If the total stored energy per unit length in the propagating wave is $\mathscr{E}'$, and the angular frequency of the fundamental mode is $\omega_{\mathrm{rf}} = 2\pi f_{\mathrm{rf}}$, the quality factor of the structure can be defined as

$$Q = \frac{\mathscr{E}'}{|dP/ds|}\omega_{\mathrm{rf}}. \tag{2.29}$$

The quality factor is a measure of the resonating quality and thereby the losses in the resonator. For a structure with a high quality factor (with a highly peaked fundamental mode), the impedance of the fundamental mode is proportional to the ratio (R'/Q).

The longitudinal loss factor per unit length k', is a quantity defined as the energy a point charge q loses to the impedance from wakefields per unit length, normalised to the charge squared. For a mode with a low group velocity the loss factor can be calculated as [15]

$$k' \equiv \frac{\mathscr{E}'}{q^2} = \frac{1}{4}(R'/Q)\,\omega_{\mathrm{rf}}, \tag{2.30}$$

and describes the losses particles see due to the mode. The energy deposited due to the impedance of the mode is converted to a wakefield trailing the charge.

2.4 Beam current and time structure

As mentioned in Section 2.3.1, the changing phase of the accelerating field requires a bunch structure of the beam, so that all particles are accelerated and not decelerated. The bunch has a certain charge q associated with it, depending on the number of particles. If the duration of a passing bunch is τ_b, then the bunch current may be defined as

$$\widehat{I} = \frac{q}{\tau_b}, \tag{2.31}$$

and is equivalent to an electrical current (charge per unit time). Some accelerators use a constant flow of bunches, while others combine several bunches into *pulses* with empty space in between. Therefore the bunches are often called *microbunches* since they form a fine substructure inside the pulse. The duration of a pulse depends on the output from the particle source of the system. The average current in one pulse is called the *pulse current* I. If T_b is the time between bunches in a pulse, the pulse curent is defined by

$$I = \widehat{I}\frac{\tau_b}{T_b} = \frac{q}{T_b}. \tag{2.32}$$

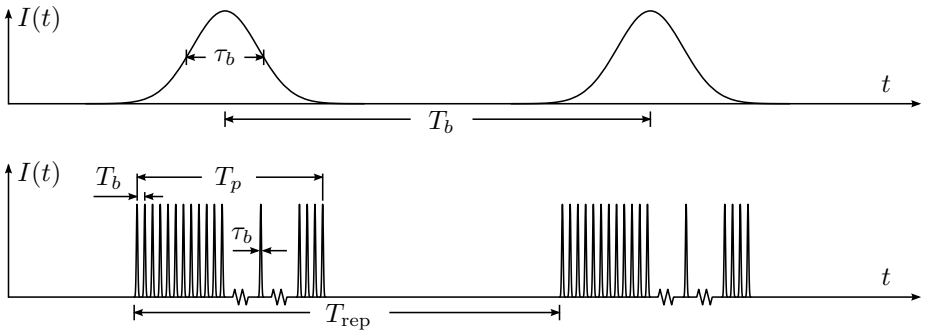

Figure 2.5: The time structure of a bunched beam. Top: Microbunches. Bottom: Pulses that are a combination of microbunches.

The inverse of the bunch spacing is the bunch frequency, $f_b = 1/T_b$. Pulses are separated in time by the repetition rate T_{rep}, and this is the inverse of the repetition frequency $f_{\text{rep}} = 1/T_{\text{rep}}$. The whole time structure with the defined parameters is shown in Figure 2.5.

The microbunch duration is related to the *bunch length*. Most particle beams have a Gaussian or near-Gaussian density distribution [9]. The bunch length standard deviation σ_z is found by multiplying with the velocity, which can be approximated with the speed of light in vacuum:

$$\sigma_z = \tau_b c. \tag{2.33}$$

Another important parameter related to the bunch length is the *charge distribution form factor*. Given a normalised longitudinal bunch charge distribution $\lambda(z)$, the form factor is the Fourier transform of it,

$$F(\lambda) \equiv \int_{-\infty}^{\infty} \lambda(\bar{z}) e^{i2\pi f_b \bar{z}/c} d\bar{z}. \tag{2.34}$$

For a symmetrical Gaussian bunch with longitudinal standard deviation σ_z, the form factor simplifies to

$$F(\lambda) = \exp\left(-\frac{1}{2}(\sigma_z 2\pi f_b/c)^2\right), \tag{2.35}$$

which is also a Gaussian function. As seen from this expression, a point-like bunch (with $\sigma_z = 0$) gives the maximum possible form factor of $F(\lambda) = 1$. The form factor is an important parameter in power production as described in Section 2.7, where it in a mathematical sense can be seen as a loss parameter due to finite bunch lengths.

2.5 Beam diagnostics

The field of accelerator physics describes in detail what happens to a particle beam in different parts of an accelerator. However, the beam is enclosed in a metallic vacuum pipe and not visible from the outside. In order to see if there is a beam present, and to measure properties of it, a wide range of instrumentation devices is used in an accelerator.

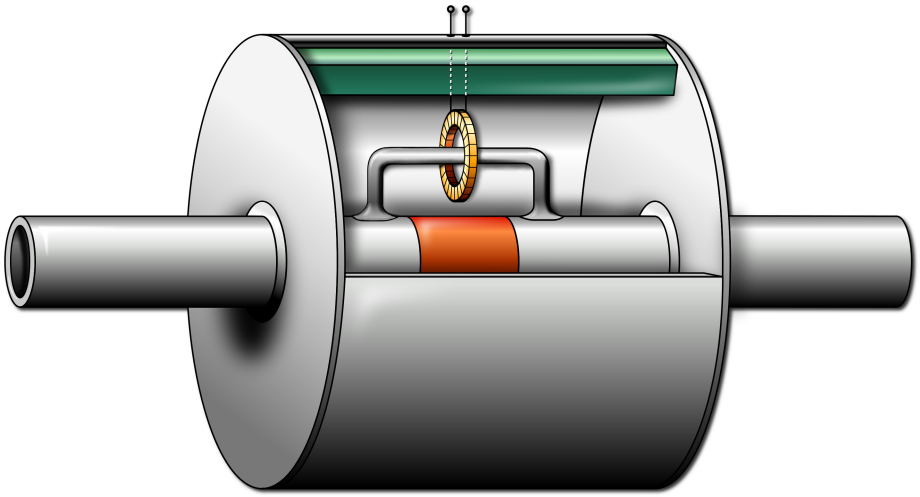

Figure 2.6: The basic principle of an inductive wall current monitor. One electrode with pick-up is shown, but real systems typically have 4 or 8 of these.

Selected methods are described here of how to measure the beam position and intensity (Section 2.5.1), the energy (Section 2.5.2), and finally the Twiss parameters and emittance (Section 2.5.3).

2.5.1 Beam position monitors

A *beam position monitor* (BPM) is a diagnostic device that is used very frequently in particle accelerators. It is used for measuring the beam intensity, and the horizontal and vertical position of the centre-of-mass of the particle bunches. The main principle of BPMs is that the charge of a bunch induces an image current on the beam pipe, and this can be measured without a large impact on the beam.

This section describes one type of BPM known as an *inductive wall current monitor* (also called *inductive pick-up*), which is the type used in the Test Beam Line. The basic principle is depicted in Figure 2.6. In the middle of the BPM the beam pipe has a ceramic gap. Because of its dielectric properties, the wall current is forced through conducting electrodes on the outside of the beam pipe. One such electrode is shown in the figure, and it goes straight through a toroidal transformer. It thereby forms the primary winding of the transformer, with one turn. The secondary winding of typically 10-30 turns [16] is led via a feedthrough to an amplifier for further processing.

The amount of wall current that flows through the electrode depends on how close the beam is to it, and this is exploited when measuring the beam position. For four electrodes that are equally spaced azimuthally, we get two output signals for each transverse plane: V_+, V_-, H_+ and H_-. The sum $\Sigma = V_+ + V_- + H_+ + H_-$ of the four signals is proportional to the beam current [17]. The difference signal $\Delta_H = H_+ - H_-$ is proportional to the horizontal position of the beam centre-of-mass, while the signal $\Delta_V = V_+ - V_-$ is proportional to the vertical position. The difference signals are divided by the sum signal since the beam current may vary. In an area in the centre of the beam pipe the signals

show a good linear behaviour and the output horizontal and vertical positions may be written, respectively, as

$$x = O_H + k_H \left(\frac{\Delta_H}{\Sigma} \right) \tag{2.36a}$$

$$y = O_V + k_V \left(\frac{\Delta_V}{\Sigma} \right), \tag{2.36b}$$

where $O_{H,V}$ are offsets and $k_{H,V}$ are linear slopes.

At the outside of the transformer there is a layer of ferrite. Its purpose is to increase the inductance in the loops between the electrodes and the body walls. This reduces the low cut-off frequency in the frequency response of the sum signal Σ, thereby giving a larger bandwidth [18]. This is important because this cut-off frequency is inversely proportional to what is called the *droop time*, and a large droop time allows for a more flat pulse signal (the signal is exponentially reduced with the droop time as time constant, and a long droop time is therefore needed to give a measurement close to the real pulse).

The advantages of the inductive wall current monitor compared to some other types of BPMs are that measurements are linear in a large part of the beam pipe, the signal bandwidths are large (4 to 6 decades) and that the sensitive parts are installed outside the vacuum pipe [19, 18].

2.5.2 Spectrometers

An easy way to measure the momentum of a particle is to let it pass through a magnetic field and observe the angle of deflection. The angle of deflection in the (x, s) plane for a particle in an infinitesimally short magnetic field is given by [2]

$$d\theta(x, s) = \frac{e}{p} B_y(x, s)\, ds, \tag{2.37}$$

where e is the charge of the particle, p is its momentum, B_y is the vertical magnetic field and ds is an infinitesimal length in the longitudinal direction. We can in general assume the use of a dipole magnet since the linear field makes the measurements much easier. To describe the total angle through a magnet, we can integrate (2.37) along the particle path, starting at a point of zero field before the magnet and ending at a point of zero field after it. The total angle is then

$$\theta_{\text{tot}} = \frac{e}{p} \int B_y(x, s)\, ds, \tag{2.38}$$

or equivalently, we have

$$p = \frac{e}{\theta_{\text{tot}}} \int B_y(x, s)\, ds. \tag{2.39}$$

The energy of the particle can then be found from the relation

$$E = \sqrt{p^2c^2 + (m_0c^2)^2}, \tag{2.40}$$

where m_0c^2 is the rest energy of the particle.

A beam will contain particles of different energies, and this is called *energy spread*. They will therefore be deflected differently according to their energies,

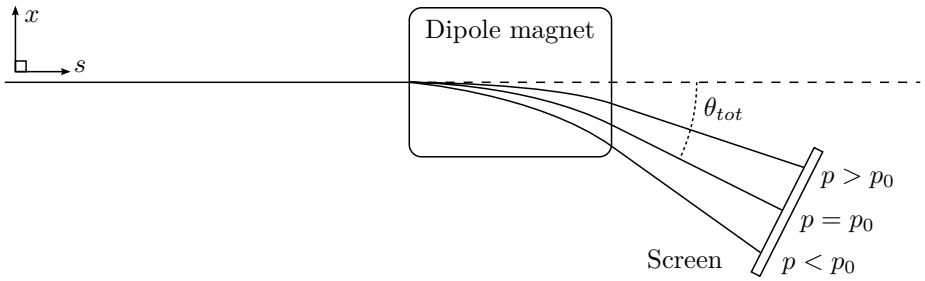

Figure 2.7: A basic spectrometer

and the whole energy spectrum can be measured with a *spectrometer*. One way to measure the energy spectrum is to use an optical transition radiation (OTR) screen imaged by a charge-coupled device (CCD) camera, and a sketch of this type of spectrometer is shown in Figure 2.7. As seen from the figure, a particle with a smaller momentum than the reference momentum p_0 is bent more, and a particle with a higher momentum than the reference is bent less. This type of spectrometer does an integrated measurement over time.

A more sophisticated method is to use several slits to separate the beam after the screen, and then measure the charge deposited as a function of time in a Faraday cup [20]. This is a *time resolved* measurement, and such a spectrometer has been designed for the Test Beam Line [21].

2.5.3 Quad scans

Knowledge of the Twiss parameters and the emittance is important to understand how the beam behaves in the accelerator. The parameters are also needed for purposes like matching as described in Section 2.1.5. A method to measure the parameters, using measurements of the transverse beam profile and a quadrupole magnet, is commonly called *quad scan*.

There are basically two ways this can be done, and both use the principle that the beam size after a focusing quadrupole decreases because of the focusing, before reaching a *waist* and then increasing again[5]. One method is to use a quadrupole with a fixed strength and measure the beam size at three or more positions (with different transport matrices), and then derive the parameters $\alpha, \beta, \gamma, \epsilon$. The other method is based on a fixed screen and a quadrupole with a changing strength, and this method will be explained here.

Consider a quadrupole and a screen downstream from it, with an arbitrary lattice in between. When the length of the quadrupole is short compared to the focal length, one may use the *thin lens* approximation and assume that $l \to 0$ in (2.11). The resulting transfer matrix for the focusing quadrupole is then

$$\mathcal{M}_F = \begin{pmatrix} 1 & 0 \\ -k & 1 \end{pmatrix}. \tag{2.41}$$

If the transfer matrix for the rest of the lattice is $\mathcal{M}_0$ with elements m_{ij}, the

[5] In principle, one only needs three different measurements, which do not need to be around the waist. However, the fit of such a data set would likely be more inaccurate.

total transfer matrix of interest is

$$\begin{aligned}\mathcal{M} &= \mathcal{M}_0\mathcal{M}_F \\ &= \begin{pmatrix} m_{11} & m_{12} \\ m_{21} & m_{22} \end{pmatrix}\begin{pmatrix} 1 & 0 \\ -k & 1 \end{pmatrix} \\ &= \begin{pmatrix} m_{11} - km_{12} & m_{12} \\ m_{21} - km_{22} & m_{22} \end{pmatrix}.\end{aligned} \tag{2.42}$$

This matrix may be used to transport the beam matrix as in (2.19), with the relation $\mathbf{\Sigma}_1 = \mathcal{M}\mathbf{\Sigma}_0\mathcal{M}^T$. By concentrating on the $(1,1)$ elements on each side, which represent the square of the beam size since $\sigma^2 = \varepsilon\beta$ from (2.17), we have

$$\begin{aligned}\varepsilon\beta_1 = m_{12}^2\varepsilon\beta_0 k^2 + (2m_{12}^2\varepsilon\alpha_0 - 2m_{11}m_{12}\varepsilon\beta_0)k \\ + (m_{11}^2\varepsilon\beta_0 - 2m_{11}m_{12}\varepsilon\alpha_0 + m_{12}^2\varepsilon\gamma_0).\end{aligned} \tag{2.43}$$

The quad scan is performed in the horizontal and vertical dimensions separately, by varying the quadrupole strength k and measuring the beam distribution on the screen. For each measurement at a fixed k, the distribution is fitted with a Gaussian curve with an offset f_0 and a peak value $f_{\max}$ as

$$f(u) = f_0 + f_{\max}\, e^{-\frac{(u-\langle u\rangle)^2}{2\langle u^2\rangle}}. \tag{2.44}$$

Here $\langle u\rangle$ is the mean, or the first moment, of the distribution, and $\langle u^2\rangle$ is the second moment of the distribution, and u can be either x or y. The second moment is equal to the square of the rms beam size and therefore also Σ_{11} of the beam matrix [22]. The fitted values for the second moment is then plotted as a function of k. It is most useful to vary k so that the plotted beam size has a minimum, which is then the waist (which occurs when the focal point is at the screen). The obtained function for the square of the beam size is then ideally a parabola, and a least squares fit can be performed [23]. Since the fitted equation and (2.43) are of the same form, the coefficients can be compared to give solutions for the Twiss parameters and the emittance at the start of the quadrupole. The Twiss parameters can then be propagated to an arbitrary position by using (2.19).

2.6 Beam steering

In practice, a particle beam will not follow the ideal trajectory through the middle of each quadrupole and BPM. For example, for a quadrupole with an offset, the beam will be closer to some poles than others and will experience a dipole field. As a result, the beam will be kicked away from the ideal trajectory, and will also experience dispersion since less energetic particles are kicked more than highly energetic particles. In addition there may be a large effect if the BPMs are offset, because the readouts will be erroneous.

The practice of guiding the beam on a good trajectory is called *steering*. In the simplest case this can be done by hand, by adjusting the strengths of corrector magnets, which are magnets that can give dipole fields in both the horizontal and vertical directions, thereby giving a kick towards the ideal trajectory. However, this is cumbersome and may take a long time.

Instead, one may use automatic steering algorithms, which can calculate the necessary kick angles from the corrector magnets, based on the readings from the BPMs. This section describes the simplest algorithm which is known as *one-to-one steering*, and which aims to center the trajectory through all of the BPMs [22]. Here it is assumed that the number of correctors is the same as the number of BPMs.

A kick θ_j at location $s = s_j$ gives an effect on the amplitude u_i at the downstream position $s = s_i$, which can be written

$$u_i = \sqrt{\beta_i \beta_j} \sin(\psi_j - \psi_i)\theta_j. \tag{2.45}$$

Here u may represent either x or y, and the amplitude is dependent on the beta function at the two positions and the difference in betatron phase. The effect from several kicks at one position add up as a superposition:

$$u_i = \sum_{j=0}^{i} \sqrt{\beta_i \beta_j} \sin(\psi_j - \psi_i)\theta_j. \tag{2.46}$$

Finally, the amplitude at all n positions from the effects of all n kicks can be written in matrix form as

$$\mathbf{u} = \mathbf{R}\boldsymbol{\theta}, \tag{2.47}$$

where $\mathbf{u} = (u_0, u_1, \ldots, u_n)$, $\boldsymbol{\theta} = (\theta_0, \theta_1, \ldots, \theta_n)$ and each element of the *response matrix* $\mathbf{R}$ can be written $R_{ij} = \sqrt{\beta_i \beta_j} \sin(\psi_j - \psi_i)$. The kick angles can be isolated from (2.47) as $\boldsymbol{\theta} = \mathbf{R}^\dagger \mathbf{u}$, where $\mathbf{R}^\dagger$ is the pseudo-inverse of $\mathbf{R}$. As the positions in $\mathbf{u}$ are known from the BPM readings, we can find the necessary angles to give zero positions by changing the sign,

$$\Delta\boldsymbol{\theta} = -\mathbf{R}^\dagger \mathbf{u}, \tag{2.48}$$

where $\Delta\boldsymbol{\theta}$ is the vector of corrector adjustments.

The one-to-one steering algorithm assumes a linear system, but can often converge for non-linear systems if used iteratively, i.e., by using (2.48) several times [6]. More advanced steering algorithms also exist, one being *dispersion-free steering* (DFS). This algorithm aims to compensate for quadrupole misalignments by minimizing the difference in trajectories for particles of different energies.

2.7 Rf power generation in PETS

To achieve the very high accelerating gradient of 100 MV/m, the CLIC scheme makes use of a novel power source called *two-beam acceleration*, where the energy of a high-intensity drive beam is extracted in *Power Extraction and Transfer Structures* (PETS), and then transferred to accelerate the main beam.

The PETS is a passive microwave device and consists of a periodically loaded waveguide. A design of the power extraction structure is shown in Figure 2.8. This is assembled from 8 copper rods into the complete structure shown to the right. As seen from the figure, the rods are *corrugated* close to the beam, and the spacing between the corrugations is related to a fraction of the wavelength of

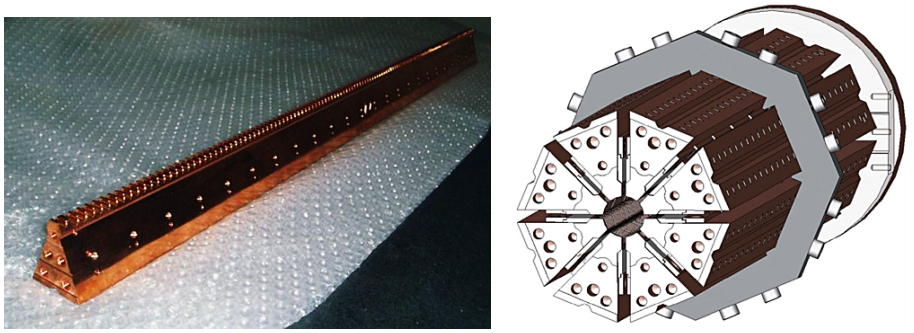

(a) One PETS rod (b) Power extraction structure

Figure 2.8: The concept of Power Extraction and Transfer Structures. (a) One PETS copper rod made for the Test Beam Line. (b) The assembled structure with all 8 copper rods. Both pictures courtesy CERN.

the bunch frequency[6], in a similar way to travelling wave accelerating structures as described in Section 2.3.2.

The passing particle bunches see the impedance of the PETS due to the corrugation, and generate a strong wakefield. The field oscillates with the fundamental mode frequency, and travels along the structure with a group velocity $v_g = \beta_g c$ that is roughly half the speed of light [24] (and therefore slower than the beam which moves with a velocity close to the speed of light). The beam can also excite higher-order modes (HOMs), which due to transverse wakes can act destructively back on the beam. Therefore, the PETS has slots with a damping material (like silicon carbide) between the rods, to lead out and damp the HOMs.

The field builds up steadily within the PETS from the contribution of several bunches, before reaching a steady state where the field is constant at the end of the structure. The field travels out of the structure through an output coupler, and can be fed into one or more accelerating structures via waveguides. A part of the fundamental mode field may continue past the output coupler, but a choke at the PETS end ensures that it is reflected back towards the output coupler.

2.7.1 Power extraction

This section provides a derivation of important formulae for power production in PETS, based on [6]. The travelling wakefield is here modelled as a field with sharply cut edges that travels with the group velocity $v_g = \beta_g c$. Furthermore, an ideal PETS output coupling and a constant bunch spacing is assumed. Finally, a damping term due to finite mode Q-values [15] is left out, and ohmic losses are incorporated in an ohmic loss reduction factor η_Ω (which for no losses is $\eta_\Omega = 1$). The fundamental mode wakefield is here simply referred to as 'the field'.

[6] In the CLIC and CTF3 schemes, the bunch frequency is 11.994 GHz, which corresponds to a wavelength of 25 mm. The current PETS design has a phase advance of 90° between the corrugations, which corresponds to a spacing of 6.25 mm.

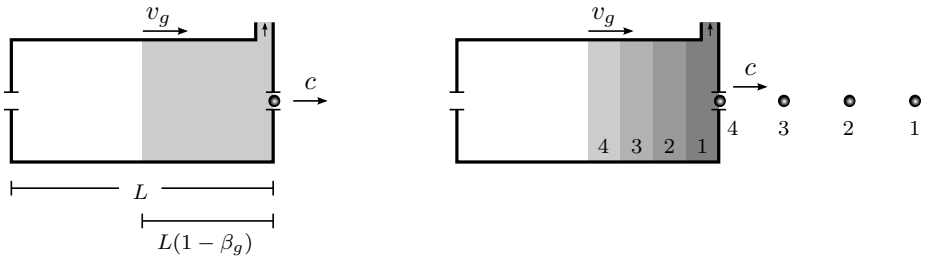

Figure 2.9: Simplified wakefield in a PETS. To the left is shown the field from a single bunch which travels with group velocity v_g, which in the illustration was set to $v_g = 0.5c$. To the right is shown the field in steady state for the same case, where one can see how far the field from each bunch has travelled. $N_{\text{fill}} = 4$ was chosen for illustrational purposes. The fields from bunches trailing bunch number 4 are not shown since they do not contribute to the field at the end.

A charge that has passed through the PETS and reached the output end, will have produced a field that due to the lower group velocity has travelled the distance $v_g L/c = \beta_g L$, where L is the PETS length. The energy in the wake field then fills a fraction $(1 - \beta_g)$ of the structure, as shown to the left in Figure 2.9. Because of this, the loss factor per unit length defined in Section 2.3.2 must be scaled with a field compression factor as [15]

$$k' = \frac{1}{4}(R'/Q)\,\omega_{\text{rf}}\frac{1}{1-\beta_g}. \tag{2.49}$$

To describe the force of the wakefield from a source particle on a witness particle, we use the longitudinal wake function per unit length $W_0'(z)$. This is defined as the average force on the witness particle per unit length, normalised to the charge of both particles. The wake function depends on the relative distance z between the particles, and for a sharply peaked mode it is given by

$$W_0'(z) = 2k' \cos\left(\frac{\omega_{\text{rf}}}{c}z\right) = \frac{1}{2}(R'/Q)\,\omega_{\text{rf}}\frac{1}{1-\beta_g}\cos\left(\frac{\omega_{\text{rf}}}{c}z\right). \tag{2.50}$$

The wake function amplitude is two times the loss factor, and that is because the loss factor describes the source particle, which only sees half of its own field [12].

Since the particles move faster than the wake field, they will eventually catch up with the field from other particles in front of them. The amplitude of the longitudinal electric field after a point-like (infinitely thin) particle bunch is equal to the wake function per unit length multiplied by the source charge q_b and the ohmic loss reduction factor η_Ω. At the location where a trailing bunch catches up with the wake, $z = 0$ and the resulting field is

$$E_\delta = q_b W_0'(0)\eta_\Omega = \frac{1}{2}q_b(R'/Q)\,\omega_{\text{rf}}\frac{1}{1-\beta_g}\eta_\Omega. \tag{2.51}$$

For a bunch with a finite length, the effective field can be found by multiplying

with the charge distribution form factor $F(\lambda)$ defined in (2.34),

$$E_{\text{bunch}} = E_\delta F(\lambda) = \frac{1}{2} q_b (R'/Q)\, \omega_{\text{rf}} \frac{1}{1-\beta_g} F(\lambda)\, \eta_\Omega. \tag{2.52}$$

The field builds up as long as trailing bunches catch up with the field of the first bunch somewhere in the middle of the structure. A steady state is reached when a trailing bunch catches up with the field of the first bunch at the PETS output, after which the extracted field will be constant. The time to reach a steady state is here defined from the time of the first rf signal at the output – which happens when the first bunch reaches the end as shown to the left in Figure 2.9 – until a bunch catches up with its field at the end of the structure. This is called the *fill time*, and is equal to the travel time of that field towards the end,

$$t_{\text{fill}} \equiv \frac{L}{v_g}(1-\beta_g). \tag{2.53}$$

The amount of bunches needed to fill the structure can then be found simply by multiplying with the bunch frequency f_b as

$$N_{\text{fill}} \equiv t_{\text{fill}} f_b = \frac{L f_b}{v_g}(1-\beta_g). \tag{2.54}$$

The field at the PETS end is a superposition of the wakes of N_{fill} bunches, so the total field can be written $E_{\text{beam}} = N_{\text{fill}} E_{\text{bunch}}$. By combining (2.52) and (2.54), and using the relation for the average current $I = q_b f_b$ over the pulse, we arrive at the equation for the steady state field

$$E_{\text{beam}} = \frac{1}{2}(R'/Q)\, \omega_{\text{rf}} \frac{L}{v_g} I F(\lambda)\, \eta_\Omega. \tag{2.55}$$

Because N_{fill} is a discrete quantity in practice, this equation will be inaccurate for small values of N_{fill} since the equation is continuous.

The field is coupled out of the PETS with a group velocity v_g. The PETS output power can be found by looking at the energy flow out of the PETS,

$$P = \frac{d\mathscr{E}}{dt} = \frac{d\mathscr{E}}{ds}\frac{ds}{dt} = \mathscr{E}' v_g. \tag{2.56}$$

Using the (R'/Q) ratio from equations (2.28) and (2.29) and rearranging, we get an expression for the stored energy per unit length,

$$\mathscr{E}' = \frac{E_{\text{beam}}^2}{(R'/Q)\, \omega_{\text{rf}}}. \tag{2.57}$$

This can be combined with (2.55) to give the expression for produced power,

$$P = \frac{1}{4}(R'/Q)\frac{\omega_{\text{rf}}}{v_g} L^2 I^2 F^2(\lambda)\, \eta_\Omega^2. \tag{2.58}$$

Here, (R'/Q) is dependent on the structure geometry, and describes the effective acceleration gradient for a given stored energy. The parameters v_g and L are also determined by the structure design, while ω_{rf} originates from the bunch frequency. The ohmic loss parameter η_Ω is a constant that should be close to

1 for CLIC [6]. The power depends on the square of the beam current I, and therefore a high drive beam current is important to provide a high power to the main beam. In addition, the power depends on the square of the form factor $F(\lambda)$, and the bunches should therefore be short.

A PETS has strict tolerances on the fabrication [5]. In the case of fabrication errors, the PETS can have a different resonance frequency than the design and the bunch frequency, and will act like a harmonic oscillator excited with a slightly wrong frequency. This is called *detuning*, and the produced power will in that case be reduced.

2.7.2 Beam deceleration

The voltage experienced by a particle of unit charge (like an electron) in a PETS corresponds to the energy loss of the particle in units of eV. Following the derivation in [6], the peak voltage at steady state can be found by integrating over the longitudinal field, and can then be expressed from the power as

$$\widehat{V} = \frac{L}{2}\sqrt{\frac{(R'/Q)\,\omega_{\mathrm{rf}}}{v_g}P}. \tag{2.59}$$

This is the voltage experienced by the most decelerated particles, while the mean voltage at steady state is given by $\langle V \rangle = \widehat{V}F(\lambda)$. The energy loss of a particle adds up as a superposition for several identical PETS.

At steady state, the CLIC drive beam will have a large energy spread, where the most decelerated particles are decelerated by 90 % after passing through all PETS. The head of the pulse, however, travels through all the PETS before the fields have built up, and will be decelerated very little. The issues of stable beam transport of such an extraordinary beam have been studied in detail in [6]. One important issue is the increase in the transverse beam size due to effects like adiabatic undamping and transverse wakes.

Another issue is that particles with different energies will experience different focusing. The focusing strategy for stable beam transport is to scale the quadrupole strengths along the lattice, so that the most decelerated particles have a constant phase advance per FODO cell [25, 26]. For CLIC, this means that the quadrupoles at the end have a strength of 10 % of the initial value.

Chapter 3

The Test Beam Line

At the heart of the CLIC scheme is the two-beam acceleration technology, where a drive beam is decelerated by up to 90 % to provide rf power for the main beam. This is a novel technology, and has a number of feasibility issues. To demonstrate a part of the technology, the CLIC Test Facility 3 (CTF3) was built with two main experiments [27], of which one is the decelerator Test Beam Line (TBL). This chapter includes a basic description of the CTF3, a detailed description of the TBL, and a section about how the PETS rf power is measured in the TBL.

3.1 The CLIC Test Facility 3

The CTF3 at CERN [27] was built to demonstrate key technologies of CLIC, and houses a drive beam generator and the CLIC EXperimental area (CLEX). An illustration of the CTF3 layout is given in Figure 3.1.

The source of the drive beam generator is a thermionic gun, which emits electrons in a continuous stream [27]. The beam then passes through a *sub-harmonic buncher* system, which in nominal operation provides a 1.5 GHz bunch structure. A linear accelerator with travelling wave structures then accelerates the beam up to 150 MeV.

Since the produced power $P \propto I^2$ as explained in Section 2.7.1, it is important to have a high beam current in order to produce a high power. A central part of the CLIC scheme is to interleave different parts of the bunch train to give one high-frequency, high-current pulse [4]. The bunch train is divided into

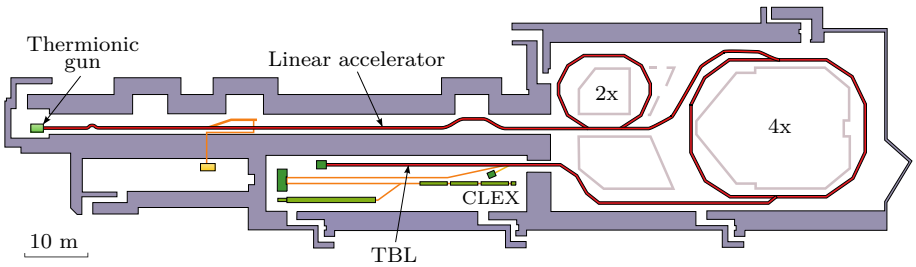

Figure 3.1: Layout of the CLIC Test Facility 3. The Test Beam Line is in the CLEX area at the bottom. Picture courtesy CERN.

140 ns sub-trains, and half of the sub-trains are sent into a *delay loop*, shown in the area to the right in Figure 3.1. After one turn they are interleaved with the other sub-trains, thereby increasing the frequency and beam current by a factor 2. This beam is then sent into a *combiner ring*, which performs a second multiplication by interleaving four sub-trains. The final pulses have a bunch frequency of 12 GHz, a current of 28 A and a length of 140 ns.

After the recombination, the beam enters CLEX. This area houses two main experiments central to the CLIC feasibility studies. One is the Two-Beam Test Stand (TBTS), which demonstrates two-beam acceleration by using the drive beam to accelerate a probe beam. The location of the TBTS and the probe beam is shown in yellow in Figure 3.1. The second experiment is the TBL, which aims to show stable transport of a heavily decelerated beam.

3.2 The TBL baseline

The main purpose of the TBL is to demonstrate the stability and efficiency of the CLIC drive beam during deceleration [28, 29]. When finalized, the main part of the TBL will consist of 16 deceleration units – each with one PETS, one inductive pick-up BPM and one quadrupole. The quadrupoles alternate between focusing and defocusing, so equivalently the periodic structure consists of 8 FODO cells.

A feature of the TBL is that the quadrupoles in the periodic structure are mounted on mechanical movers, which can move the magnets horizontally and vertically with a precision of 5 μm [30]. This allows the quadrupoles to be used as correctors for efficient beam steering, since the beam also experiences a dipole field when it has an offset through a quadrupole [9]. There are also 3 conventional corrector magnets in the lattice.

The whole TBL lattice with 16 PETS is shown in Figure 3.2. However, most PETS are not yet installed, and are shown as dashed symbols. The beam enters from the top in the figure, and the first dipole magnet can send the beam to either the TBL or the TBTS. A further option is to send the beam to a spectrometer for energy measurements. After being decelerated in the main part of the lattice in the TBL, the beam is then sent to a spectrometer at the end of the line. Quad scans can be performed at the beginning and at the end of the line, by using movable OTR screens at the positions shown in the figure. These measurements can give an indication of the emittance growth in TBL, and are also needed for matching.

The nominal parameters for the TBL beam are shown in the upper part of Table 3.1, while the PETS structure parameters are shown in the lower part. With these parameters, each PETS will according to (2.58) produce a steady state power of

$$P = 139 \text{ MW}. \tag{3.1}$$

Following the derivation in Section 2.7, the peak voltage seen by the beam is

$$\widehat{V} = 5.20 \text{ MV}. \tag{3.2}$$

After travelling through all 16 PETS, the most decelerated particles will then have an energy of

$$E_{\min} = E_0 - 16\, e\widehat{V} = 67 \text{ MeV}, \tag{3.3}$$

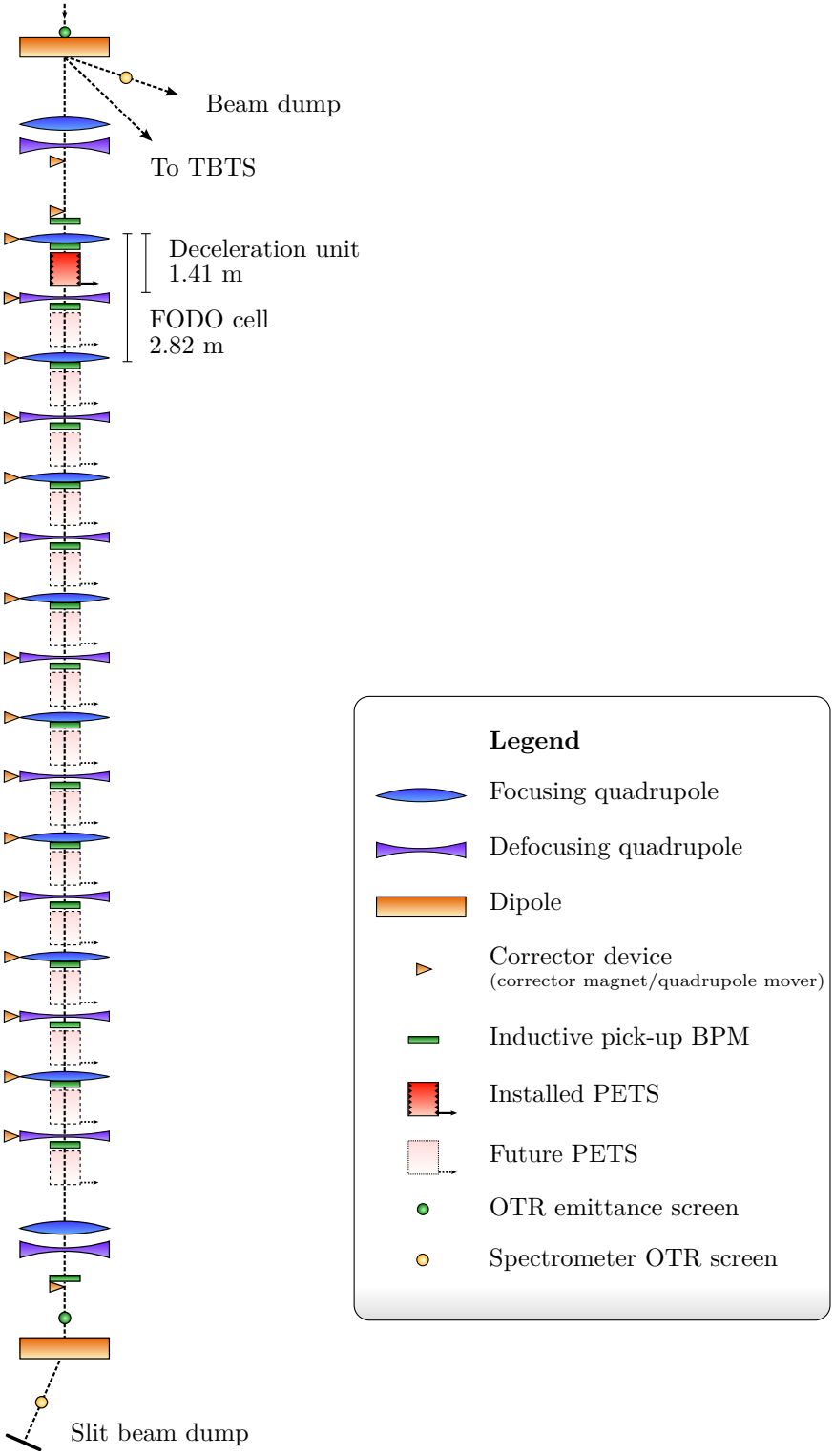

Figure 3.2: The TBL lattice. Focusing/defocusing refers to the horizontal plane.

Table 3.1: Nominal parameters for the TBL.

Symbol	Beam parameters	Value	Unit
E_0	Initial energy	150	MeV
$E_{\min}$	Minimum final energy	67	MeV
η_{extr}	Energy extraction efficiency	55	%
q	Bunch charge	2.3	nC
σ_z	Bunch length	1.0	mm
$F(\lambda)$	Bunch form factor	0.969	-
f_b	Bunch frequency	11.994	GHz
T_b	Bunch spacing	83	ps
T_p	Pulse duration	140	ns
I	Pulse current	28	A
$\varepsilon_{Nx}, \varepsilon_{Ny}$	Initial normalised emittances	150	μm
T_{rep}	Repetition rate	1.2	s
Symbol	**PETS parameters**	**Value**	**Unit**
f_{rf}	Fundamental mode frequency	11.994	GHz
(R'/Q)	Fundamental mode impedance	2222	linac-Ω/m
β_g	Fundamental mode group velocity	0.46	c
L	Length	0.8	m
η_Ω	Ohmic loss factor	0.985	-
t_{fill}	Fill time	3.1	ns

and the energy extraction efficiency for the TBL can be defined as

$$\eta_{\text{extr}} = \frac{E_0 - E_{\min}}{E_0} = 55\ \%. \tag{3.4}$$

The TBL is a prototype of the CLIC decelerator, but some parameters are of course different [5]. For instance, the CLIC drive beam current is 101 A, which is almost a factor 4 higher than for TBL. However, the CLIC PETS length is 0.21 m (roughly $\frac{1}{4}$ of the TBL PETS length), and therefore the power produced per PETS is of the same order. If we calculate the energy extraction efficiency for CLIC we arrive at 90 % [6], but the TBL studies with 55 % deceleration is still expected to be a good demonstration. It should be noted that the minimum final energy of CLIC is 240 MeV, which is higher than the initial energy in the TBL.

3.3 Current status

By autumn 2010, all magnets, quadrupole movers and diagnostics have been installed in the TBL, as well as one PETS. A picture of the current setup is shown in Figure 3.3a. The nominal parameters with one PETS give a maximum of 5.2 MeV energy loss, while the precision of the spectrometry is on the order of a few MeV. Therefore, most of the beam time has so far been used for conditioning and power production experiments. The schedule is to install 7 more PETS during 2011 and the remaining 8 in 2012 [31].

The installed PETS was manufactured by CIEMAT [32], and is placed within

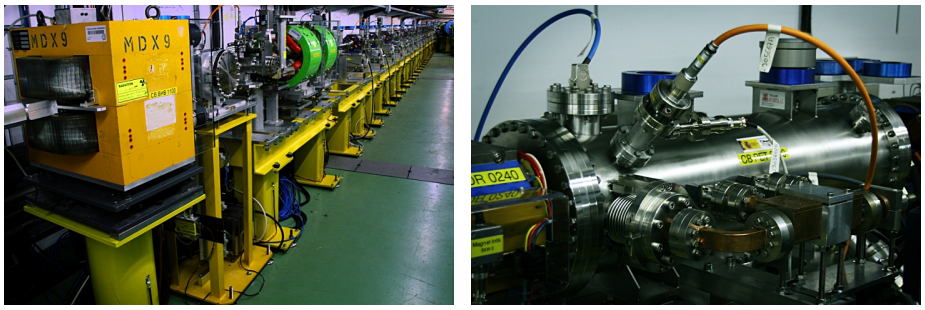

(a) The TBL (b) The first installed PETS

Figure 3.3: (a) The Test Beam Line, seen from the dipole at the end. (b) The first installed PETS tank in the TBL.

a vacuum tank as shown in Figure 3.3b. Due to a detuning of -50 MHz in the synchronous frequency, a loss of ca. 10 % is expected in the power produced [33].

The CTF3 beam can be set up to bypass the delay loop and/or the combiner ring, thereby giving different combination schemes. The TBL has so far been operated with beam currents ranging from $2.5 - 17$ A, with a maximum PETS power of 50 MW. The initial beam energy is ca. 114 MeV [1].

The two installed spectrometers are equipped with OTR screens, and can be used for integrated average energy and energy spread measurements. A segmented beam dump will be installed early 2011, which will provide a time resolved energy spread measurement, with an accuracy of about 5 % [21, 34].

The bunch profile can presently not be measured in the TBL, but a *streak camera* will be set up early 2011 [35] which will allow for this type of measurement. However, a recent measurement in the combiner ring [36] gave bunch lengths of $\sigma_z = 1.5 - 2.9$ mm. This is higher than the nominal bunch length and gives a smaller form factor, which in turn gives a smaller PETS power amplitude since $P \propto F^2(\lambda)$.

3.4 Methods of power measurements

A central part of the operation of the TBL is to measure the produced rf power in the PETS. The measured power can be compared to predictions based on (2.58) and the BPM current signals. This section aims to explain how the power is measured in the first installed PETS.

As described in Section 2.7, the beam induces a strong wakefield in the PETS, and roughly half of the field is coupled out on each side of the PETS in two output couplers. The availability of two output couplers – called *arms* – allows for measuring asymmetries in the field. Ideally the field on each side should be similar, if only the monopole wake due to the fundamental mode is present. Field asymmetries can originate from effects like dipole wakes.

The power in each PETS arm is roughly half of the produced power, which for nominal parameters is 70 MW. The utilized electronics operate in the milliwatt

[1] The accelerator is powered by rf amplifiers called *klystrons*, and 8 out of 10 klystrons in CTF3 are currently in operation. Therefore the energy is currently lower than the nominal.

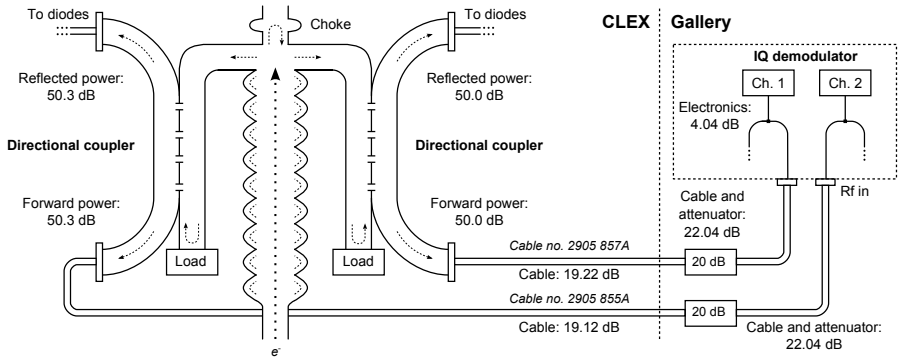

Figure 3.4: A diagram of the PETS power signal chain, with signal attenuation in different parts.

range, so the field must be coupled to a cable and heavily attenuated before the signal enters the electronics. This is done in a series of passive microwave components, which will hereby be denoted the *signal chain*.

An illustration of the signal chain for the installed PETS is given in Figure 3.4. The electron beam enters the PETS from the lower left. The induced wakefield travels along the structure and out of the two output couplers at the sides, while a choke ensures that the fundamental mode field does not follow the beam further.

Each PETS arm is terminated in a water load. A directional coupler with several coupling slots is connected to each arm, and the forward power and the reflected power are coupled to separate cables. The average dissipated power from the cables is very low compared to the 70 MW peak because the duty cycle $T_p/T_{\text{rep}} \approx 10^{-7}$ (cfr. Sections 2.4 and 3.2). The reflected power is ideally small since little should be reflected from the load. The amplitude of the reflected power is measured with a network of Schottky diodes.

For the forward power, not only the power amplitude but also the phase information is relevant, and the measurement is therefore done with an IQ demodulator. The forward power, which is ideally produced at the combined bunch frequency of 11.994 GHz, is mixed with a local oscillator operating at the same frequency. There are two resulting frequency components (one at the difference between the two frequencies and one at the sum), but the high-frequency component is filtered out. Therefore, one will ideally have a DC signal at the in-phase (I) and quadrature (Q) channels in the steady state of the beam pulse. Small deviations in the bunch frequency can however lead to low-frequency sinusoidal signals at the I and Q outputs. Calibration factors are applied separately to the I and Q channels, before the channels are combined into amplitude and phase signals.

The attenuations in different parts of the signal chain can be seen in Figure 3.4. By adding up the forward power attenuation for each arm, we arrive at 95.5 dB for the left arm and 95.3 dB for the right arm. The components are measured separately, and the differences originate from small fabrication errors. The measurement accuracy due to the heavy attenuation is estimated [7] to be 10 %.

3.4.1 Calibration of the IQ demodulator

The PETS forward power from the two arms is measured in two IQ demodulators. Due to electronics imperfections, some parameters must be accounted for:

- Offsets in the I and Q signals
- Amplitude difference between the I and Q signals
- Phase deviation from 90° between the I and Q channels (which is the ideal value)

A calibration of the IQ demodulator was therefore done, and the procedure is given in appendix B.

The calibration values were found to have drifted after a few months, and therefore 3 new calibrations were done over 3 weeks. The difference in the measured power for each arm for the different calibrations was within $2-3$ % (depending on the amplitude ratio between the I and Q channels), and therefore the values were assumed to be stable. The updated values are also given in the appendix, and these are used in the calculations in Chapter 5.

Chapter 4

The TBL graphical user interface

To operate the TBL and to perform the relevant measurements and experiments, a graphical user interface (GUI) was developed in Matlab [37]. The interface displays monitoring information and automatizes tasks like matching and steering.

The GUI is divided into three parts that deal with different modes of operation or experiments, of which two have been developed. These parts are denoted *user screens*, and the program shows one of them at a time. The user can switch between the screens by using designated buttons. The first user screen displays measurements on the beam and is used for matching and steering. The second screen is used for measurements and experiments with one PETS. The third screen is yet to be developed, and will deal with deceleration experiments with several PETS.

The program is started from Matlab in the CTF3 control room, and is normally run on Linux. This chapter describes the functionality of the different user screens and how the program is used in normal operation of the TBL.

4.1 Optics, matching and steering

The first user screen is used for monitoring, matching and steering for the TBL. It therefore allows the operators to efficiently transport the beam through the lattice. This screen is shown at the startup of the program, and a screenshot is shown in Figure 4.1. The buttons for switching between the different user screens are at the top left.

In the middle of the screen one can see the lattice, which should be compared to Figure 3.2. The quadrupoles are shown as optics lenses with focusing related to the horizontal plane, while correctors and PETS have different symbols. However, the figure in the GUI also shows a part of the lattice before the TBL, since the quadrupoles there are used for matching, as described below. The beam enters from the left, so the starting point in Figure 3.2 is at the brown dipole to the left.

The lattice figure is drawn at the startup of the program, with information from a file that contains the optics model. This file is output from the matching

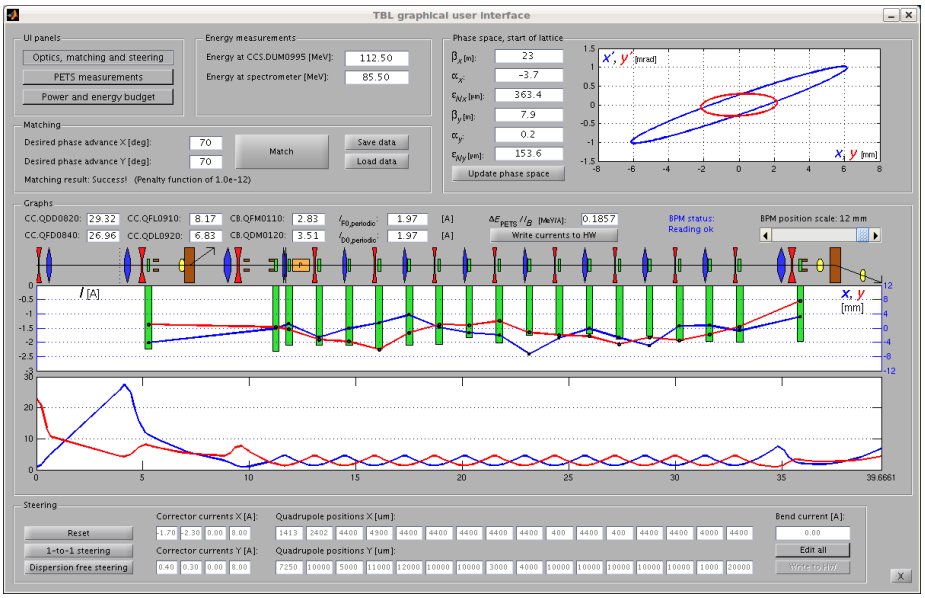

Figure 4.1: The GUI screen for optics, matching and steering. A larger version of the figure is provided in Appendix D.

algorithm described below. In this way, the longitudinal positions and lengths in the figure are correct with respect to the technical drawings. However, the effective magnet lengths and not the physical lengths are shown. If the lattice is changed, e.g., when more PETS are installed, the changes only need to be applied in the optics model.

Below the lattice figure is the BPM display, which is updated with the pulse repetition time $T_{\text{rep}} = 1.2$ s. The mean values over the pulse of the current and position signals are read from the control system, and displayed under the relevant BPMs in the lattice figure. The beam current is shown with green bars, and is defined in CTF3 to be negative because of the charge of the electron beam. The horizontal and vertical mean position signals are shown with blue and red lines, respectively. Since it can be of interest to look at the positions with different scales, a slider above the lattice figure allows to adjust the scale shown to the right with values ranging from ± 0.03 to ± 15 mm.

A total of 57 BPM signals is read every cycle. The normal option of reading the signals one by one with Matlab was found to be too slow, as the total time exceeded the repetition time. Therefore, a stand-alone Java application[1] is used for reading the BPMs. This application runs in the background, and is called with a `system` command at startup. The Java application writes the data to text files, which are read by the GUI and plotted every cycle. In some cases the readings are not updated, for instance at the startup of the Java application. Therefore, the GUI checks if the timestamps in the text files are updated, and then displays a status of the readings.

Spectrometer measurements and quad scans are normally done with automated Matlab scripts (not written by the author). The results are kept in a

[1] The Java application has been developed by Tobias Persson at CERN.

text file which is read at the startup of the GUI. The measured energies at the beginning and end of the TBL are then displayed in the top center, while the Twiss parameters and the emittances are displayed in the top right. If the measurements are done while the program runs, the values can be updated from the text boxes. These measurements are used for matching and steering, as described below.

In the top right corner of the user screen, the phase space ellipses are shown for both transverse planes. The ellipses are based on the values from the quad scan, which is taken close to the dashed line shown in the lattice figure. They therefore act as a visual display of the beam at the start of the line.

4.1.1 Matching interface

A part of the first user screen is used for matching as described in Section 2.1.5. The matching of the TBL optics is done with an interface to the optics code MAD-X [11], which has built-in matching procedures. The main panel for matching can be seen at the left and close to the top in Figure 4.1.

The user has one free parameter in the matching process, and that is the betatron phase advance per FODO cell in the periodic structure. In a FODO structure, the betatron motion performs periodic oscillations. When the horizontal and vertical emittances are equal, the ideal phase advance per FODO cell is 90°, since that gives the smallest beam size [9]. The user can however adjust the phase advance, with a possibility of having different values for the two transverse planes.

The phase advance is related to the transport matrix of the FODO cell. The phase advance can therefore be changed by adjusting the quadrupole currents, which in turn control the magnet strengths. If the transport matrix for one plane has elements $m_{11}, m_{12}, m_{21}, m_{22}$, the phase advance can be expressed as [2]

$$\phi = \arccos\left(\frac{m_{11} + m_{22}}{2}\right). \tag{4.1}$$

Due to the non-linear algebraic equation that is obtained, the equation is solved numerically for the quadrupole strengths that give the specified phase advance in the periodic structure.

The matching is performed in the middle of the first quadrupole in the periodic structure. In this position, the beta function for one transverse plane have a maximum and the beta function in the other transverse plane has a minimum [9]. Thus $\alpha = -\frac{1}{2}\beta' = 0$ in both planes. The beta function in one plane can be expressed from (4.1) as

$$\beta = \frac{m_{12}}{\sin\phi}. \tag{4.2}$$

When the user presses the 'Match' button in the GUI, a number of parameters are written to a text file. First of all, this includes the betas from (4.2) for both planes, which are used as constraints by the matching script. Furthermore, the script defines the FODO quadrupoles with the currents that were found numerically. Finally, the beam energy read from the GUI and the Twiss parameters and emittances at the start of the lattice are included. Since the Twiss parameters and emittances are known at a different position than the start, they are first transported back via transport matrices by using (2.19).

After the text file is written, the MAD-X script is called with a `system` command, and reads the text file. The matching is done with 6 constraints. Four of them are the specified values of $\alpha_x, \beta_x, \alpha_y, \beta_y$ in the middle of the first quadrupole in the periodic structure. The two remaining specify a maximum value for the beta functions in a small region[2]. There are also 6 variable parameters in the matching algorithm, which are quadrupoles currents. The currents are allowed to vary within the possible range of the magnets.

When the matching is finished, the values of the 6 quadrupole currents are written to a text file, read by the GUI and displayed in the text boxes above the lattice figure. In addition, a *penalty value* from MAD-X is displayed below the match button. This value can be seen as the error between the ideal and the current solution, and should ideally be as small as possible. A threshold of 10^{-10} was set in the program to categorize whether a matching was successful or not.

Another file is also generated by MAD-X, which contains a table with the calculated beta functions along the lattice, together with the positions. The beta functions are read by the GUI and plotted below the BPM display. As seen from Figure 4.1, the solution shows a periodicity in the periodic FODO structure.

If satisfied with a matching solution, the user can set the currents of the real magnets. This is done automatically with the 'Write to HW' button, where HW denotes hardware.

4.1.2 Steering interface

At the bottom of the first user screen is a panel for steering, described in Section 2.6. As explained in Section 3.2, there are 16 quadrupoles and 4 corrector magnets that can be used for steering in the TBL. A text box is shown for each of these elements for both transverse planes, and there is also a text box for the current of the dipole at the end of the TBL.

The steering interface has a *read mode* and a *write mode*, and the switching between these is done with the 'edit all' button. Read mode is used from the start of the program, and in this mode the program polls the control system continuosly for the corrector and dipole currents and quadrupole positions. The text boxes are set to read-only in this mode.

In write mode, the text boxes become editable, and are not updated with new values from the control system. The values can then be changed manually. When satisfied, the user can send the values to the hardware with the 'Write to HW' button.

After the magnets have been set, there is a probability that the transmission of the beam gets worse. Therefore, the previous magnet currents are remembered from the time of entering write mode, and stored in a file. By clicking the 'reset' button on the left, the old values can be read from the file and reapplied.

There is also a possibility for automatic 1-to-1 steering, by using the designated button to the left. The steering algorithm in Section 2.6 must be changed somewhat, since the quadrupoles and correctors affect the beam differently when the energy is changed by deceleration, and because one needs to take into account transverse effects in the PETS. The program therefore uses an interface

[2]The beta functions found by the matching algorithm were often very high in a certain region, and the beam size would then be too large for the beam pipe.

to the tracking code PLACET [38] to calculate a response matrix for the lattice. The beam current and energy are written to text files, which are read by PLACET after it is called by a `system` command. The response matrices are then written to files that are imported into the GUI.

The steering is done using (2.48), with the calculated response matrices and the BPM position signals read from the control system. The resulting $\Delta\theta$ in the two planes describe the differences in kick angles from the current values, needed to steer the beam through the center of the BPMs. These angles are proportional to the corrector currents and the quadrupole positions. Therefore, after some scaling the values are added to the currents and positions read by the control system. The new values are written to the text boxes, and the interface is set to write mode. This allows the user to inspect the values and possibly make changes, before deciding whether to write the values to the hardware or not.

There is also a button for dispersion-free steering (DFS) in the interface, but the code has not been implemented. It can be of interest to experiment with DFS in the future, so the code can possibly be added in a future version of the program.

4.1.3 Regular use for beam transport

To illustrate how the GUI is used in regular operation, we can look at the different steps needed for efficient beam transport. The first user screen is normally used from the start of the TBL beam time, to set up the optics and guide the beam through the TBL.

Usually, a spectrometer measurement and a few quad scans are first done at the start of the lattice. The parameters are written to the text file used by the program, and the program is started.

The matching algorithm is then started with the 'Match' button. Phase advances of 90° are used for both planes from the start and usually give good matching results. When a successful match has been performed, the operator checks whether the magnet strengths look reasonable, and can then automatically set the magnets.

The final step for transporting the beam is steering. This can either be done with a few minor adjustments (if there is already a good transmission), or by running the 1-to-1 steering algorithm.

4.2 PETS measurements screen

The second user screen is developed for power production experiments with the first installed PETS in the TBL. A screenshot is shown in Figure 4.2.

At the top of the screen is a panel for the theoretically predicted power produced by the PETS. The power production formula is displayed in the middle of the panel, and is based on (2.58) with an extra reduction factor due to a detuning of the PETS [33]. The user can adjust the form factor and the detuning with text boxes, and see how this affects the power prediction. The predicted power and energy loss is shown to the right. The program uses the average beam current from the BPM downstream of the PETS in the calculation. The rest of the parameters are structure parameters and are not subject to change.

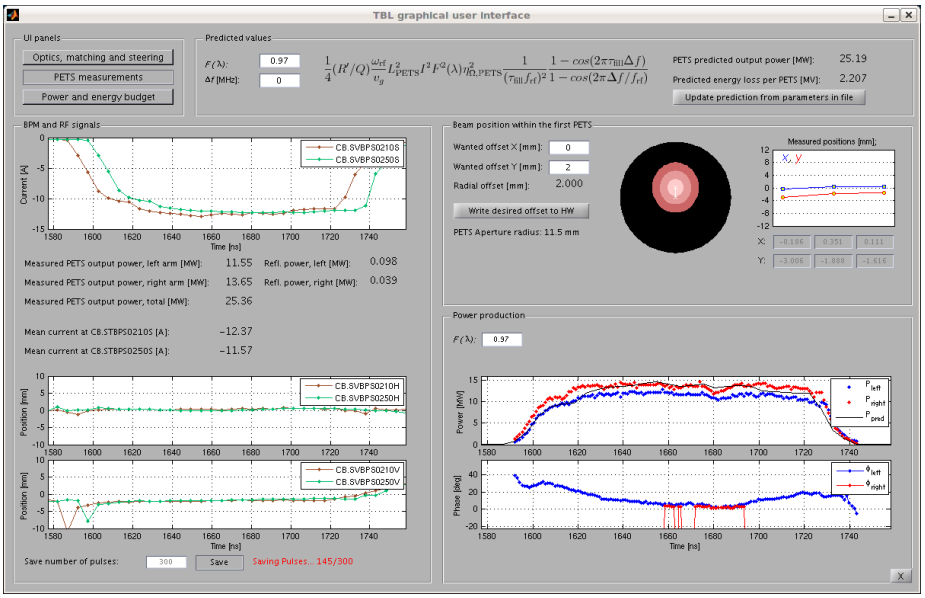

Figure 4.2: The GUI screen for PETS measurements and experiments. A larger version of the figure is provided in Appendix D.

They are therefore read from a text file at the startup of the program. In case the text file is changed while the program is running, it can be read again by using the 'Update predictions from parameters in file' button.

4.2.1 BPM pulse display

The left part of the user screen is mainly used for displaying BPM pulses (and not only the means as in Figure 4.1). All signals on this panel are updated with the repetition time $T_{\text{rep}} = 1.2$ s. It is important for the power production to know if the beam is well transported through the PETS, and therefore the uppermost graph shows the BPM current signals from just before and just after the PETS (in brown and green, respectively). The horizontal position signals for the same BPMs are shown in the graph in the middle, while the vertical position signals are shown at the bottom. These two graphs give an indication of the beam position through the PETS. As seen from Figure 4.2, the measured position is -2 mm in the vertical plane.

Since the timing of the electronics sometimes change, an edge detection algorithm is run each cycle to detect the left and right edges of one of the current signals. This is done by simply searching for the first sample above the noise floor. All three BPM signal graphs then show the time window from the result, since the signals are on the same electronics crate and therefore have the same timing. Since the beam current can range from $1 - 28$ A, the ordinate axis of the current display is also scaled automatically.

Numerical values for the beam current in the two BPMs are shown above the position graphs. The values are averages taken over the steady state part of the pulses (based on the edges detected). The same algorithm is used to show numerical values for the forward power amplitudes. The forward power

signals are shown in the panel in the lower right corner, as described below. The reflected power value shows the peak amplitude.

At the bottom of the BPM panel is an interface for saving signals. The user can specify a number of pulses, and by clicking on the 'Save' button, the program saves the signals for each pulse in a separate Matlab file. The saved signals are BPM pulses and raw IQ signals with timestamps, as well as additional signals that are of interest for conditioning the CTF3 machine. The saving progress is shown next to the button, and there is a possibility to turn off the saving process by clicking the button a second time.

4.2.2 Beam steering in the PETS

The panel to the right on the user screen is used for steering the beam through the PETS, with a constant position offset from the axis. This type of steering is relevant for the experiments in Section 5.2. By using the two text boxes on the left, the user can specify a certain horizontal and vertical position offset through the PETS. The resulting radial offset is then shown underneath.

For this type of measurement, it is important to transport the beam through the PETS without losing much of the beam to the beam pipe. A figure therefore shows the beam position and the available PETS aperture. The three pink circles represent one, two and three standard deviations of the beam distribution for the transverse planes, while the black circle shows the aperture. The beam size is based on the values from the quad scan on the first user panel, transported to the beginning of the PETS using (2.19).

When the user clicks the 'Write desired position to HW' button, the program steers the beam with the specified offset through the PETS. To have positions different from zero, (2.48) can be modified as

$$\Delta\boldsymbol{\theta} = \mathbf{R}^{\dagger}(\mathbf{u}_{\mathrm{req}} - \mathbf{u}_{\mathrm{meas}}), \tag{4.3}$$

where $\mathbf{u}_{\mathrm{req}}$ is the specified positions and $\mathbf{u}_{\mathrm{meas}}$ is the measured positions in one plane. To analyze the effect of the offset on the power production, the clearest test is to have a constant position offset. Thus, the two BPMs just before and just after the PETS are used, and $\mathbf{u}_{\mathrm{req}}$ contains two elements with the same value, as specified by the user. As an example, for Figure 4.2 this vector would be

$$\mathbf{x}_{\mathrm{req}} = \begin{bmatrix} 0 \\ 0 \end{bmatrix} \qquad \text{and} \qquad \mathbf{y}_{\mathrm{req}} = \begin{bmatrix} 2 \\ 2 \end{bmatrix} \tag{4.4}$$

for the two planes. The two corrector magnets before the PETS are used to give the kicks (cfr. Figure 3.2).

The graph on the right of the steering panel shows the measured mean positions, and displays the signals of the two BPMs used for this steering algorithm as well as the one upstream. Numerical values are displayed underneath the graph. After the steering has been done, the two last values should therefore ideally show a constant position for each plane. The operator can see if the values improve when doing the steering in an iterative way.

4.2.3 Power production display

The panel to the lower right is used for displaying the measured PETS power, and the signals are updated with the pulse repetition time T_{rep}. The uppermost

graph in the panel shows the measured forward power amplitude in the two PETS arms in blue and red. In addition, a predicted curve based on (2.58) is displayed in black, using the current signal from the BPM before the PETS. The form factor in the prediction can be changed in the text box above the graph, and this allows for a quick estimation of the form factor and therefore the consistency of the signals and the power production.

The BPM and power signals have different timings and sampling rates, but since edge detection is performed on both types of signals, the left edges are fitted together on the time axis.

The lowermost plot shows the phases from the power measurements for the two PETS arms. There is generally an offset in the absolute phase between the two signals, because of the different cable lengths. Therefore, one signal is moved so that it is displayed on top of the other. The ordinate axis is scaled automatically, so that only the phase variation along the pulse is shown (and not the high noise values where the amplitude is zero).

Chapter 5

PETS Power production experiments

An essential part of the TBL experiment is to understand the power production in the PETS. Section 5.1 gives a general discussion of the rf power measurements and how this compares to the theoretical expectations. In Section 5.2, an experiment is described in which the effect of the beam position on the produced power is analyzed.

5.1 Measurements and predictions

As described in Sections 2.7 and 3.4, the PETS produces rf power due to the wakefield induced by the beam, and the power in the two PETS arms is measured with IQ demodulators. An example of the measured power for one pulse can be seen in Figure 5.1, where the power along the pulse in the left PETS arm is shown in blue, and the power in the right arm is shown in red. As seen in the figure, the total power amplitude is ca. 20 MW, which was produced with an 11 A beam. The right plot shows the relative phases of the fields for the same signals.

5.1.1 Form factor estimations

The produced power can in addition to the measurements be predicted using (2.58) and the measured beam current. This is done by using the current signal of a BPM adjacent to the PETS. In this context, the form factor can be seen as a free parameter, and when the prediction is fitted together with the measurements one can get an estimation of the form factor. Consulting Figure 5.2, we can see the relation between the form factor and the bunch length, and how it affects the power production. The green curve shows how the amplitude of the PETS power changes due to the form factor.

One way to do the estimation is to manually adjust the form factor in the calculation until the curves agree. By using the parameters from Section 3.2 with (2.58), we obtain

$$P = (1.87 \times 10^5)\, F^2(\lambda)\, I^2. \tag{5.1}$$

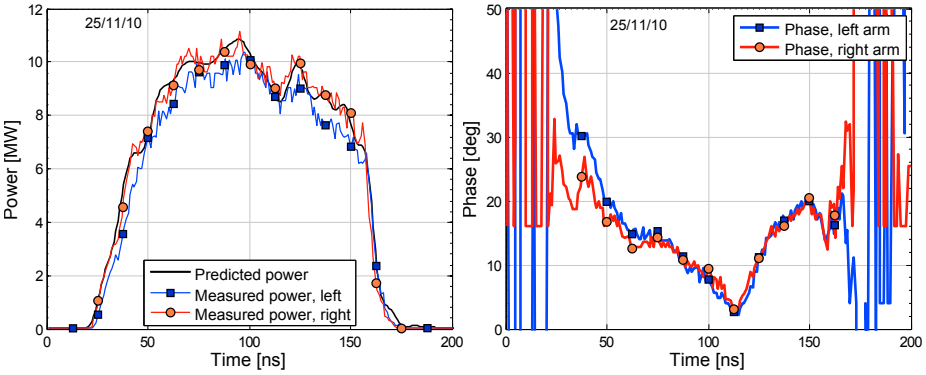

(a) Power amplitude (b) Phase of the power

Figure 5.1: Power production. (a) Amplitude of the rf signal, shown for the two PETS arms in blue and red, and the predicted power shown in black. (b) Phases of the rf signal, where the blue and red curves represent the two arms.

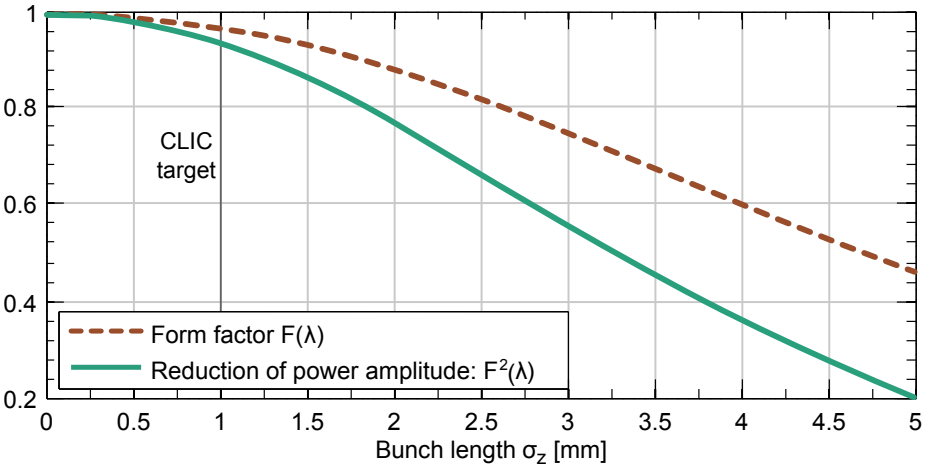

Figure 5.2: Relation between the bunch length and form factor. The brown stapled curve shows the form factor as a function of the bunch length, and the green curve shows the resulting reduction in the amplitude of the power.

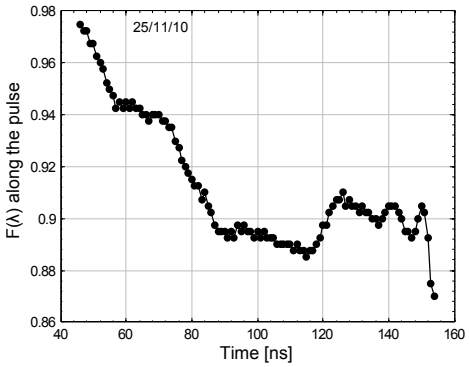

Figure 5.3: A fit of the form factor along the pulse, for the same measurements series as in Figure 5.1.

This method is fast and can be done online in the TBL GUI, as described in Section 4.2.3. Such a prediction is shown in Figure 5.1, where the black line represents the predicted power. A form factor of $F(\lambda) = 0.90$ was used in this case.

Another option is to do a fit by minimizing the rms difference between the curves. By doing this minimization over a large number of pulses, one may reduce effects from noise and imperfections that vary over time. Since the bunch lengths and phases may vary, it is also informative to fit the form factor along the pulse, by minimizing the rms difference for each sample. Such a fit is shown in Figure 5.3, where 300 pulses were used in the calculation. The obtained form factor is high in the first part of the pulse, but then drops because the measured power is less than the prediction.

The form factor estimations can be compared with *streak camera* measurements in the combiner ring, which allows for measuring the bunch lengths. These measurements [36] generally correspond to $F(\lambda) \approx 0.8$. The fitted form factor in TBL is generally higher than these measurements, with values ranging from $F(\lambda) = 0.80$ to more than 1 (however, values higher than 1 do not have a physical meaning). This can originate from various calibration errors in the system[1]. Another possible explanation is bunch compression in the transport line from the combiner ring to CLEX, but if present this is likely a small effect. A summary of typical form factor estimations for different dates is given in Table 5.1.

5.1.2 Power production used for machine conditioning

There is a lot of elements in CTF3 that affect the beam and have an influence on the experiments in CLEX. In particular, the recombination scheme requires fine-tuning of the delay loop and the combiner ring to achieve a constant bunch spacing. The information from the power production has been a valuable tool for conditioning the rest of the machine, so that the beam is optimized for the experiments.

[1] Even though the calculations in Appendix B show good agreements, they only apply to the IQ demodulator at the end of the rf signal chain. There may also be erroneous measurements for the rest of this chain, or errors in the BPM calibration.

Table 5.1: Typical estimated form factors for different dates in 2010. Form factors higher than one are not physically possible, and might indicate signal calibration errors.

Date	**23/08**	**24/08**	**01/09**	**23/09**	**29/09**	**07/10**	**04/11**
$F(\lambda)$	1.0	1.05	0.94	0.97	0.97	1.04	0.80
Date	**11/11**	**19/11**	**22/11**	**23/11**	**25/11**	**26/11**	
$F(\lambda)$	0.90	0.93	0.90	1.0	0.90	0.90	

One diagnostic that has been used is the estimation of the form factor, by using plots such as Figures 5.1a and 5.3. Ideally, the form factor should have a constant high value over the pulse to allow for efficient power production. The operators can therefore use the form factor estimations to optimize the delay loop and combiner ring.

Another diagnostic is the phase signals from the IQ demodulators, as seen in Figure 5.1b. The machine can be optimized while inspecting the phase signals, since a variation in the bunch phases reduces the power production [33].

5.2 Correlations of power and beam position

In CLIC, the PETS will produce a power of 135 MW which is used to accelerate the main beam [5]. The delivered field and phase affects the energy gain of the main beam, and the final energy of the main beam affects the collision rate at the interaction point [39]. It is therefore essential that the PETS power is kept constant under different drive beam conditions.

The drive beam might be slightly offset in the CLIC decelerators due to misalignment of the lattice elements [6], and one relevant experiment is to study how the position of the drive beam influences the produced power. Ideally, if only the fundamental mode is present, the wake field is constant even if there is an offset in the beam position from the axis [12]. Therefore, the field in the two arms should be independent of the beam position. However, higher-order modes (HOMs) can be excited when the beam is off-axis.

An experiment was done in the TBL where the beam was steered with different position offsets through the PETS, while several hundred pulses were logged with the GUI for each offset. The measurements were done with a beam of $10 - 12$ A and a total PETS power of ca. 25 MW. Nine measurements series were taken, at the following approximate offsets from the axis:

(a) No offset (the beam was centered on the axis)
(b) -4 mm horizontal offset
(c) -2 mm horizontal offset
(d) $+2$ mm horizontal offset
(e) $+4$ mm horizontal offset
(f) -3 mm vertical offset
(g) -2 mm vertical offset
(h) $+2$ mm vertical offset
(i) $+3$ mm vertical offset

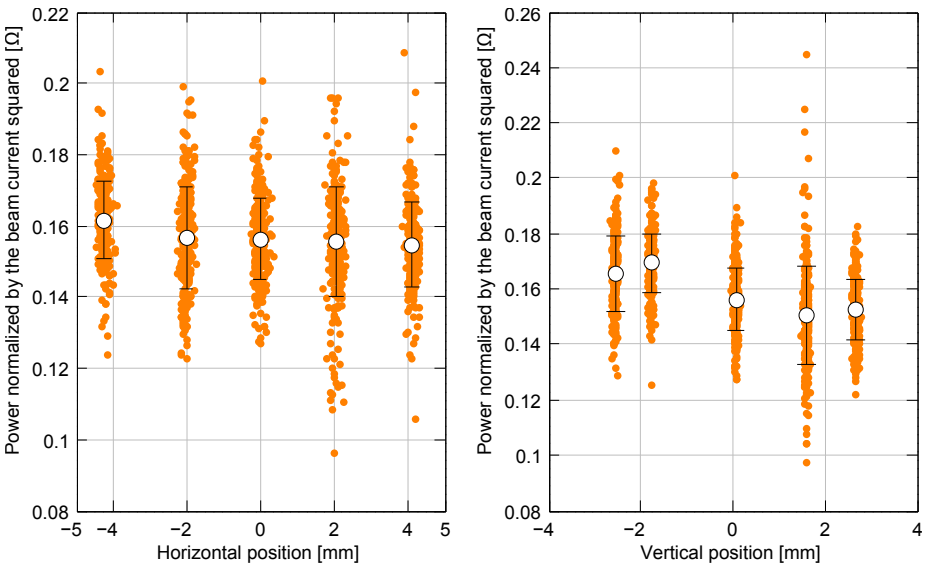

Figure 5.4: The total PETS power normalised by the beam current squared. The left plot shows the power plotted against the horizontal position offset, while the right plot shows the power plotted against the vertical position offset. The white circles with error bars represent the means and standard deviations.

Figure 5.4 shows the total power for both PETS arms, plotted against the position for all measured pulses. Since the power strongly depends on the beam current like $P \propto I^2$, the power is normalised by the measured current squared to take out effects of current variations. The power is calculated as an average over a part of the steady state of the pulse, and the BPM current signal is averaged over the same time window. The horizontal and vertical positions are calculated as the average of the BPM signals from just before and just after the PETS (over the same time window). In case of a slightly diagonal beam path, the abscissa axes therefore represent the beam position between the middle of the PETS and the output coupler.

The five measurements series related to the horizontal offset (a–e) are shown in the left plot, while the five measurements series related to the vertical offset (a and f–i) are shown in the right plot (the series with no offset is shown in both). The means of the measurements series are shown as white circles, while the error bars represent the standard deviations. As seen from the figure, the total power appears to be independent of the beam position, which agrees with the theory.

5.2.1 Power in the two PETS arms

For the same measurements series, the ratio between the power in the two PETS arms was plotted against position, and the result is shown in Figure 5.5. Again, the left plot shows the effect of the horizontal position while the right plot shows the effect of the vertical position. The ordinate axis shows the power in the left arm divided by the power in the right arm. The values are smaller than unity since the measured power in the right arm is constantly higher, likely due to

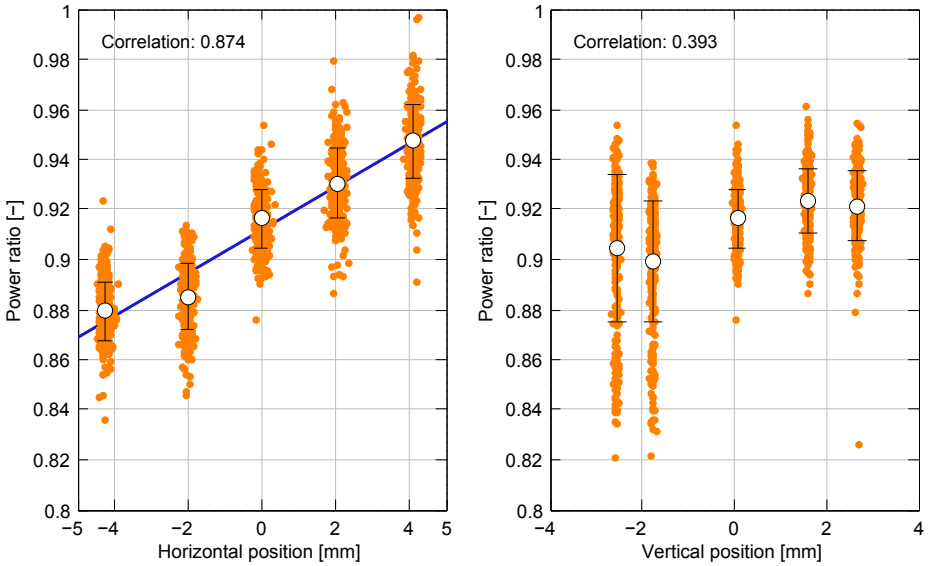

Figure 5.5: The ratios between the power in the left and right PETS arms, plotted against the beam position. The white circles with error bars represent the means and standard deviations. A linear fit is shown in blue for the horizontal case.

calibration errors [40].

No clear trend can be seen in the right plot in Figure 5.5, indicating that the vertical position has limited effect on the output field distribution. However, by inspecting the left plot, we can see a dependence on the horizontal position, which is unexpected. To investigate this behaviour further, we can calculate correlation coefficients between the ratio and different powers of the horizontal and vertical positions. A strong linear dependence on the horizontal position is found from the data, with a correlation coefficient of 0.874. A linear fit is shown in blue in Figure 5.5.

For completeness, we may also investigate if a part of the beam was lost in the structure. The beam transmission through the PETS is plotted in Figure 5.6, and is calculated as the average beam current in the BPM just after the PETS, divided by the average beam current in the BPM just before the PETS. Concentrating on the left plot, we see that the three middle points show a very good transmission while the two extreme points show ca. 1 % losses.

5.2.2 Changes in phase

In CLIC, the power from two PETS arms will be combined in a *matched T-junction* [40]. If the phases of the two incoming fields are different, the fields will not be perfectly combined and a part is reflected back towards the PETS.

It is therefore relevant to study the phase behaviour due to the beam position. The absolute phases depend on cable and waveguide lengths, but if the difference between the phases from the two arms is constant, the fields can be combined correctly by using the proper waveguide lengths before the T-junction.

Figure 5.7 shows the difference between the two phase signals, plotted against

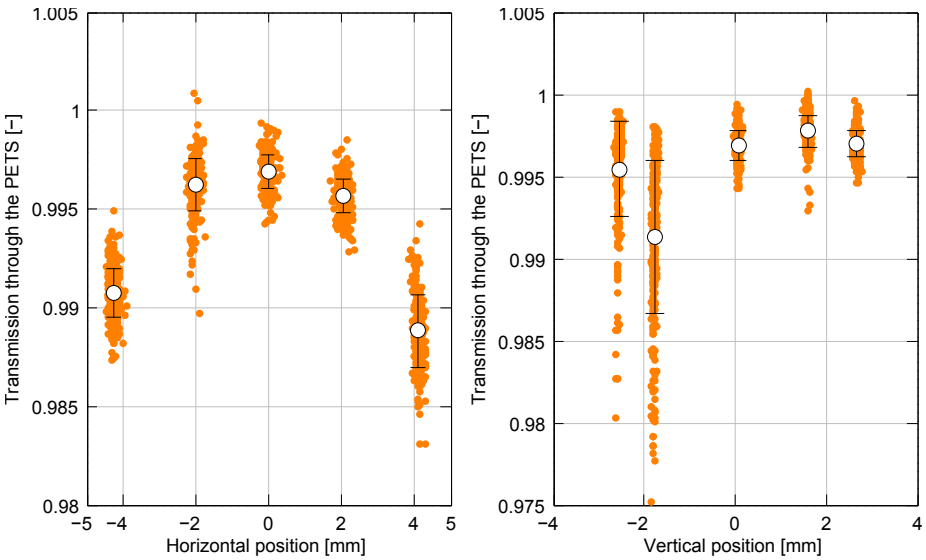

Figure 5.6: Beam transmission through the PETS, plotted against the position. The white circles with error bars represent the means and standard deviations.

the position. The average difference over the pulse is shown, for the same time window used earlier. As seen from the figure, the variation due to the beam position is small. The non-zero phase difference in the figure originates from the different cable lengths in the measurements.

5.2.3 The effect of the beam position and future work

From Figures 5.4 and 5.5, we see that the total PETS power is unaffected by the beam position inside the structure, while the ratio between the power in each arm changes linearly with the horizontal position. This may be an issue for CLIC, because the fields from the two arms may not combine perfectly, and a part of the field may be reflected.

These results are unexpected for the time being, and need to be investigated further. A relevant study would be to run rf simulations of the output coupler. In addition, the PETS could be simulated with an offset beam, to study the distribution of fields inside the structure. To investigate the presence of HOMs in the PETS, one could also measure the frequency spectrum of the PETS arms and look for peaks other than at the fundamental mode frequency.

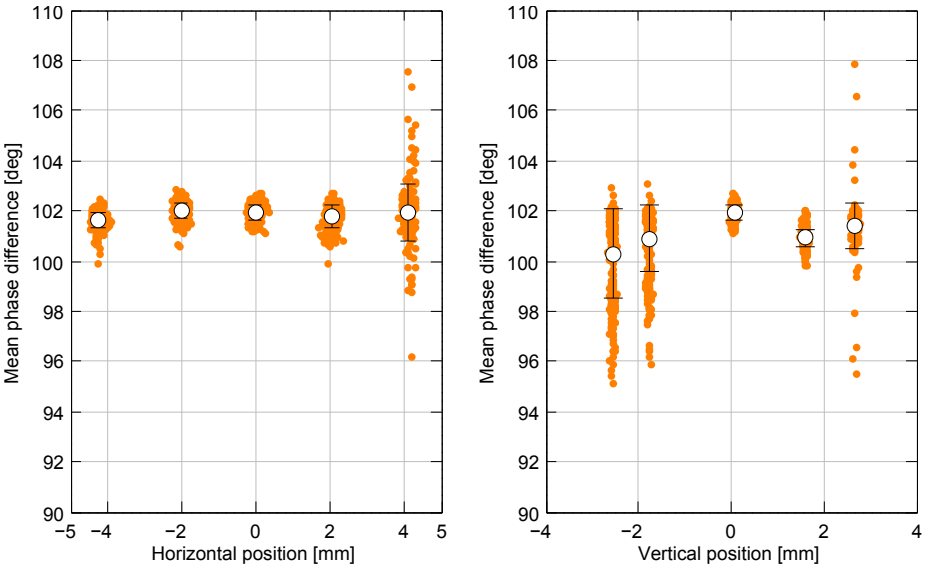

Figure 5.7: The average difference between the phase signals in the two PETS arms, plotted against the position. The white circles with error bars represent the means and standard deviations.

Chapter 6

Conclusion and outlooks

This thesis has studied the CTF3 Test Beam Line and in particular power production experiments in PETS. Understanding the PETS power production is vital for the feasibility of the proposed electron-positron collider CLIC.

The TBL is the first prototype of the CLIC decelerator, and has been described in detail. In particular, the first installed PETS and the methods of power measurements have been documented. As an essential tool for performing the operation and experiments, a GUI was developed specifically for the TBL. The program was written in Matlab, with interfaces to the optics code MAD-X and the tracking code PLACET. The program has been described in detail, including the methodology of the calculations and the signal readings.

A part of the GUI was designed for power production experiments, and the results of these experiments have been analyzed. A relevant experiment was performed where the correlation of power production and beam position inside the PETS was investigated. The results show that the total power and the difference between the phases are independent of the beam position. However, the power coupled out on each side of the PETS depends on the horizontal beam position, and the ratio between the power on each side shows a linear trend. This dependence is not fully understood.

It is recommended to further investigate the asymmetry of the power distribution. For CLIC, it is important that the field is correctly combined and transferred to the main beam. An incorrect accelerating field in the main linac affects the gradient, and can lead to a reduced collision rate at the interaction point. One relevant experiment could be to study the frequency spectrum in the PETS arms, to search for potential HOMs. One might also run simulations, for instance to study how the difference in fields affect the high power rf network used to feed the main beam.

When the TBL is finalized, the effects of many PETS on the beam can be studied. The produced power along the line can then be compared to the theory, and this can also be compared to deceleration measurements from spectrometers. The TBL should ultimately demonstrate a stable transport of a heavily decelerated beam, which is one of the feasibility issues for CLIC.

The thesis has provided more insight into rf power production. In particular, it has been pointed to matters that agree or differ from the expectations, which should be further analyzed in order to investigate if they affect the CLIC feasibility issues.

Bibliography

[1] "Information at the official CERN web page." `http://public.web.cern.ch/public/en/About/`.

[2] K. Wille, *The Physics of Particle Accelerators, an introduction.* Oxford University Press, 2000.

[3] J. Brau, Y. Okada, and N. Walker, eds., *International Linear Collider Reference Design Report.* ILC Global Design Effort and World Wide Study, 2007.

[4] G. Guignard, ed., *A 3 TeV e+e- Linear Collider based on CLIC Technology.* CERN, 2000.

[5] "CLIC parameter table." Available online at `http://clic-meeting.web.cern.ch/clic-meeting/clictable2010.html`.

[6] E. Adli, *A Study of the Beam Pysics in the CLIC Drive Beam Decelerator.* PhD thesis, University of Oslo, 2009.

[7] E. Adli, A. E. Dabrowski, S. Döbert, M. Olvegård, D. Schulte, I. Syratchev, and R. L. Lillestøl, "Experimental program for the CLIC Test Facility 3 Test Beam Line," in *Proceedings of the 1st International Particle Accelerator Conference, IPAC'10*, 2010.

[8] D. J. Griffiths, *Introduction to Elementary Particles.* Wiley, second ed., 2008.

[9] H. Wiedemann, *Particle Accelerator Physics.* Springer, third ed., 2007.

[10] H. Goldstein, C. Poole, and J. Safko, *Classical Mechanics.* Addison-Wesley, third ed., 2002.

[11] W. Herr, "A MAD-X primer," in *Proceedings of the CAS - CERN Accelerator School: Intermediate Course on Accelerator Physics*, pp. 505–528, CERN, 2006.

[12] A. Chao, *Physics of Collective Beam Instabilities in High Energy Accelerators.* Wiley-Interscience, 1993.

[13] D. M. Pozar, *Microwave Engineering.* Wiley, third ed., 2005.

[14] O. Bruning, P. Collier, P. Lebrun, S. Myers, R. Ostojic, J. Poole, and P. Proudlock, eds., *LHC Design Report.* CERN, 2004.

[15] P. B. Wilson, "High energy electron linacs: Application to storage rings rf systems and linear colliders." SLAC-PUB-2884 (Rev.), 1991.

[16] P. Forck, P. Kowina, and D. Liakin, "Beam position monitors," in *Proceedings of the CAS - CERN Accelerator School: Course on Beam Diagnostics*, pp. 187–228, CERN, 2009.

[17] J. J. García Garrigós, *Design and Construction of a Beam Position Monitor Prototype for the Test Beam Line of the CTF3*. PhD thesis, Universidad Politécnica de Valencia, 2008.

[18] M. Gasior, "An inductive pick-up for beam position and current measurements," in *Proceedings of the 6th European Workshop on Beam Diagnostics and Instrumentation for Particle Accelerators, DIPAC'03*, pp. 53–55, 2003.

[19] J. J. García-Garrigós, A. Faus-Golfe, and J. V. Civera-Navarrete, "Design and construction of an inductive pick-up for beam position monitoring in the test beam line of the CTF3," in *Proceedings of the 11th biennial European Particle Accelerator Conference, EPAC'08*, pp. 1110–1112, 2008.

[20] T. Lefèvre, H. H. Braun, E. Bravin, C. Dutriat, and C. P. Welsch, "Segmented beam dump for time resolved spectrometry on a high current electron beam," in *Proceedings of the 8th European Workshop on Beam Diagnostics and Instrumentation for Particle Accelerators, DIPAC'07*, pp. 340–342, 2007.

[21] M. Olvegård, A. Dabrowski, T. Lefèvre, S. Döbert, and E. Adli, "Time resolved spectrometry on the Test Beam Line at CTF3," in *Proceedings of the 9th European Workshop on Beam Diagnostics and Instrumentation for Particle Accelerators, DIPAC'09*, pp. 257–259, 2009.

[22] M. G. Minty and F. Zimmermann, *Measurement and Control of Charged Particle Beams*. Springer, 2003.

[23] M. C. Ross, N. Phinney, G. Quickfall, H. Shoaee, and J. C. Sheppard, "Automated emittance measurements in the SLC," in *Proceedings of the 1987 IEEE Particle Accelerator Conference, PAC'87*, pp. 725–728, 1987.

[24] I. Syratchev, D. Schulte, and E. Adli, "High rf power production for CLIC," in *Proceedings of the 22nd IEEE Particle Accelerator Conference, PAC'07*, pp. 2194–2196, 2007.

[25] H. H. Braun and R. C. et al., eds., *The CLIC RF power source – A novel scheme for two-beam acceleration for electron-positron linear colliders*. CERN, 1999.

[26] J. A. Riche, "Maximum energy transfer efficiency in CLIC drive beam and proposal for a method of focusing, derived from a very general discussion on focusing in linacs." CERN CLIC Note 266, 1994.

[27] G. Geschonke and A. Ghigo, eds., *CTF3 Design Report*. CERN, 2002.

[28] D. Schulte and I. Syratchev, "Considerations on the design of the decelerator of the CLIC Test Facility (CTF3)," in *Proceedings of the 21st IEEE Particle Accelerator Conference, PAC'05*, pp. 1177–1179, 2005.

[29] S. Doebert, G. Rumolo, D. Schulte, I. V. Syratchev, and D. Carrillo, "Progress on the CTF3 Test Beam Line," in *Proceedings of the 10th biennial European Particle Accelerator Conference, EPAC'06*, pp. 783–785, 2006.

[30] F. Toral, C. Burgos, D. Carrillo, J. L. Gutierrez, I. Rodriguez, E. Rodríguez, S. Sanz, C. Vazquez, J. Calero, L. García-Tabarés, E. Adli, N. Chritin, S. Doebert, and J. A. Rodriguez, "Design, manufacturing and tests of a micrometer precision mover for CTF3 quadrupoles," in *Proceedings of the 11th biennial European Particle Accelerator Conference, EPAC'08*, pp. 1517–1519, 2008.

[31] E. Adli, S. Döbert, R. Lillestol, M. Olvegaard, I. Syratchev, D. Carrillo, F. Toral, A. Faus-Golfe, J. J. Garcia-Garrigos, Y. Kubyshin, and G. Montoro, "Commissioning status of the decelerator test beam line in CTF3," in *Proceedings of the 25th Linear Accelerator Conference, LINAC'10*, 2010.

[32] F. Toral, D. Carrillo, P. Abramian, F. Aragon, J. Calero, L. Garcia-Tabares, J. L. Gutierrez, A. Lara, E. Rodriguez, L. Sanchez, S. Doebert, and I. Syratchev, "Manufacturing and testing of a TBL PETS prototype," in *Proceedings of the 1st International Particle Accelerator Conference, IPAC'10*, pp. 3768–3770, 2010.

[33] E. Adli, "Drive beam bunch train phases and TBL power production." Presentation CLIC Beam Physics Meeting, November 2010.

[34] M. Olvegård, E. Bravin, F. Carra, N. Chritin, A. Dabrowski, A. Dallocchio, S. Döbert, T. Lefèvre, and E. Adli, "Spectrometry in the Test Beam Line at CTF3," in *Proceedings of the 1st International Particle Accelerator Conference, IPAC'10*, pp. 1113–1115, 2010.

[35] A. Dabrowski. Private communication.

[36] A. E. Dabrowski, E. Adli, S. Bettoni, R. Corsini, S. Döbert, T. Lefèvre, A. Rabiller, L. Soby, P. K. Skowronski, F. Tecker, D. Egger, M. Velasco, and H. Shaker, "Measuring the longitudinal bunch profile at CTF3," in *Proceedings of the 25th Linear Accelerator Conference, LINAC'10*, 2010.

[37] "MATLAB by MathWorks." Online at `http://www.mathworks.com/products/matlab/`.

[38] "The tracking code PLACET." Online at `https://savannah.cern.ch/projects/placet/`.

[39] D. Schulte, "Consideration on the conceptual phase stabilization system." Presentation at the CLIC meeting 08/10/10.

[40] S. Döbert. Private communication.

List of Figures

2.1 The phase space ellipse in the (u, u') plane 10
2.2 A charged particle and the resistive beam pipe wake 13
2.3 A cylindrical pillbox cavity 14
2.4 A basic travelling wave structure with iris-shaped screens. 15
2.5 The time structure of a bunched beam 17
2.6 The basic principle of an inductive wall current monitor 18
2.7 A basic spectrometer 20
2.8 The concept of PETS 23
2.9 Simplified wakefield in a PETS 24

3.1 Layout of the CLIC Test Facility 3 27
3.2 The TBL lattice 29
3.3 Photos of the TBL and the first installed PETS tank 31
3.4 The PETS power signal chain 32

4.1 The GUI screen for optics, matching and steering 35
4.2 The GUI screen for PETS measurements and experiments 39

5.1 Power production, amplitude and phase 43
5.2 Relation between bunch length and form factor 43
5.3 Fit of the form factor along the pulse 44
5.4 Total normalised PETS power vs. position 46
5.5 Ratios between power in each PETS arm vs. position 47
5.6 Transmission through the PETS vs. position 48
5.7 Difference in phase vs. position 49

Appendix A

List of abbreviations

Abbrv.	Meaning	Section
BPM	Beam Position Monitor	2.5.1
CERN	The European laboratory for particle physics (originally Conseil Européen pour la Recherche Nucléaire)	1.1
CLEX	CLIC EXperimental area	3.1
CLIC	Compact Linear Collider	1.2
CTF3	CLIC Test Facility 3	3.1
DFS	Dispersion-Free Steering	2.6
FODO	Focusing and Defocusing	2.1.2
GUI	Graphical User Interface	4
HOM	Higher-Order Mode	2.3.1
HW	Hardware	4.1.1
IQ	In-phase and Quadrature	3.4
LHC	Large Hadron Collider	1.1
OTR	Optical Transition Radiation	2.5.2
PETS	Power Extraction and Transfer Structure(s)	2.7
RF	Radio Frequency	2.3
TBL	Test Beam Line	3
TBTS	Two-Beam Test Stand	3.1

Table A.1: A list of abbreviations in the thesis. The meaning of the abbreviations are given together with the section in which they are defined.

Appendix B

Calibration of the PETS IQ demodulator

The next pages of this appendix contains a document that was written after the first calibration of the IQ demodulator in May 2010. The procedure of the measurements and post-analysis is explained, and the calibration parameters are listed in tables.

A few months after this calibration was done, the measurements setup was believed to have drifted, so three new calibrations were done over three weeks. The new calibration parameters are given in Table B.1, for the IQ channels used for the first PETS (channels 1 and 2). This table should be compared to Table 3 in the document.

Using the formula for P_{out} in the document, the maximum difference between two sets of parameters is 1.83 % when the I and Q amplitudes are equal (with the parameters from 23/09/10 and 29/09/10). The maximum possible difference occurs when the I channel is zero and the Q channel has a finite value, and that difference is 2.83 %.

Table B.1: New calibration values for the IQ demodulator, for three different dates for channels 1 and 2. Offsets in the I and Q channels are denoted O_I, O_Q.

		O_I [mV]	O_Q [mV]	ϕ [rad]	N	Slope
Ch. 1	23/09/10	1.17	-6.55	0.0556	0.987	0.172
	29/09/10	1.14	-7.07	0.0497	0.990	0.171
	07/10/10	0.88	-6.73	0.0529	0.984	0.172
Ch. 2	23/09/10	1.19	-6.07	0.0607	0.980	0.152
	29/09/10	0.87	-6.46	0.0588	0.973	0.150
	07/10/10	0.90	-6.06	0.0570	0.974	0.151

Reidar L. Lillestøl, 20/05/10

Calibration of the TBL IQ demodulator

This document contains the calibration measurements for the IQ demodulator for the TBL. Settings were at first a nominal frequency of 11.994 GHz from the synthesizer and a power of 0 dBm. The electronics for the IQ demodulator are shown in Figure 1.

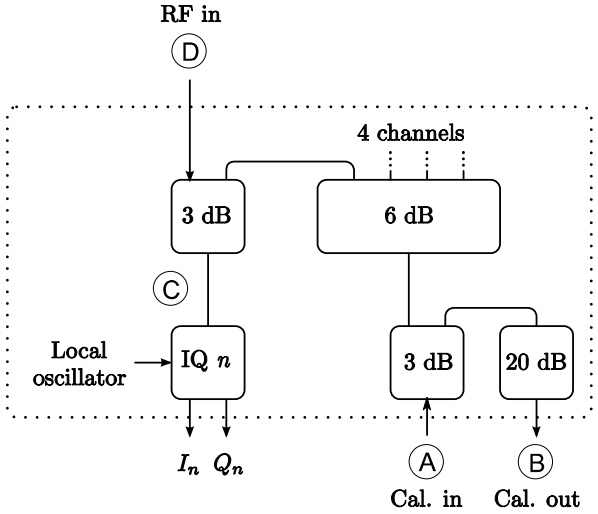

Figure 1 - Electronics for the IQ demodulator

At first, four power measurements were taken between different ports:

i. Loss in the synthesizer and power meter cables was measured by connecting the synthesizer directly to the power meter.
ii. The synthesizer was connected to the cal. in port (A in the figure) and the power meter was connected to the cal. out port (B in the figure). The signal then passed through a 3 dB splitter and a 20 dB attenuator.
iii. The synthesizer was connected to the cal. in port (A) and the power meter was connected at point C in the figure. The signal then passed through two 3 dB splitters and one 6 dB splitter.
iv. The synthesizer was connected to the RF input port (D) and the power meter was connected at point C in the figure. The signal then passed through one 3 dB splitter.

These four measurements were taken once for channels 1-4 and once for channels 5-8. This is because different cal. in ports are used for the two cases, but else there should not be any difference between the 8 individual channels. All these measurements are given in Table 1.

Table 1 - Loss measurements in the electronics

MEASUREMENT	(i)	(ii)	(iii)	(iv)
Channels 1-4	-1.47 dB	-25.75 dB	-16.04 dB	-5.51 dB
Channels 5-8	-1.23 dB	-25.88 dB	-17.11 dB	-5.09 dB

The box with the IQ demodulators was then fixed in the rack. The total measured calibration attenuation (as in point ii) was then -25.86 dB for channels 1-4.

Calibration of channels 1 and 2

The local oscillator (operating at 11.9942 GHz) was connected to the "LO in" port before the IQ demodulators, and the synthesizer frequency was changed to 11.9992 GHz (5 MHz above, so that the mixed output frequency was 5 MHz). The 4 channels in Acqiris card 3 were now:

1. I channel 1
2. Q channel 1
3. I channel 2
4. Q channel 2

The 4 channels were read from the Oasis scope with Matlab and stored, for a number of different input powers from the synthesizer. In addition, the power meter readings were noted. The synthesizer powers and power meter readings are given in Table 2.

Table 2 - Synthesizer powers and corresponding power meter readings

Input power [dBm]	-10	-8	-6	-4	-2	0	2	4
Power meter reading [dBm]	-36.13	-34.03	-32.00	-30.03	-28.00	-26.10	-24.10	-22.14

Input power [dBm]	6	8	10	12	14	16	18	
Power meter reading [dBm]	-20.20	-18.22	-16.28	-14.34	-12.38	-10.41	-9.56	

Data post processing

The stored curves did not have an integer number of periods. To be able to correct for offsets correctly (by subtracting the means), an algorithm was made to truncate the curves at an integer number of periods. This was done by first making a smoothed version of the curves to reduce noise, and then search backwards along each curve for a value within 1.5 % of the value at sample number 20. Sample 20 was chosen instead of sample 1 since the smoothing filter average over fewer samples on the edges of the signal (and the signal will thus contain more noise there). The algorithm also verified that the curve at the chosen truncation point moved in the same direction as the curve at sample 20. The search was done for all 4 channels individually, and then the median of the four truncation points was taken to correct for eventual erroneous values. Finally, the original signals were truncated outside this sample number and sample 20.

Offsets were corrected in all 4 channels individually by subtracting the means of the signals. The amplitudes of the signals were found by calculating the RMS values and multiply them by $\sqrt{2}$. The angle deviations from 90° between *I* and *Q* channels were found with the following formula:

$$\varphi = \sin^{-1}\left(2\frac{\overline{I_C Q_C}}{A_I A_Q}\right)$$

where A_I and A_Q are the amplitudes of one *I* and one *Q* channel, and the mean is taken of the product of the corresponding signals I_C and Q_C, that are corrected for offsets. A normalisation factor *N* was calculated from the ration of the two amplitudes, that is $N = A_I / A_Q$. The output powers were finally calculated as

$$P_{out} = I_C^2 + \left(\frac{N}{\cos\varphi}Q_c - I_C \tan\varphi\right)^2$$

The input powers were calculated by subtracting attenuation measurement (ii) from the power meter

readings and adding attenuation measurement (iii), and then converting from dBm to mW. The output power as a function of the input power (in logarithmic scale) and the input power as a function of the output power (in linear scale) are shown in Figure 2. As can be seen, the curves are quite linear. Linear fits were made on the curves on the right, and they can hardly be distinguished from the original curves.

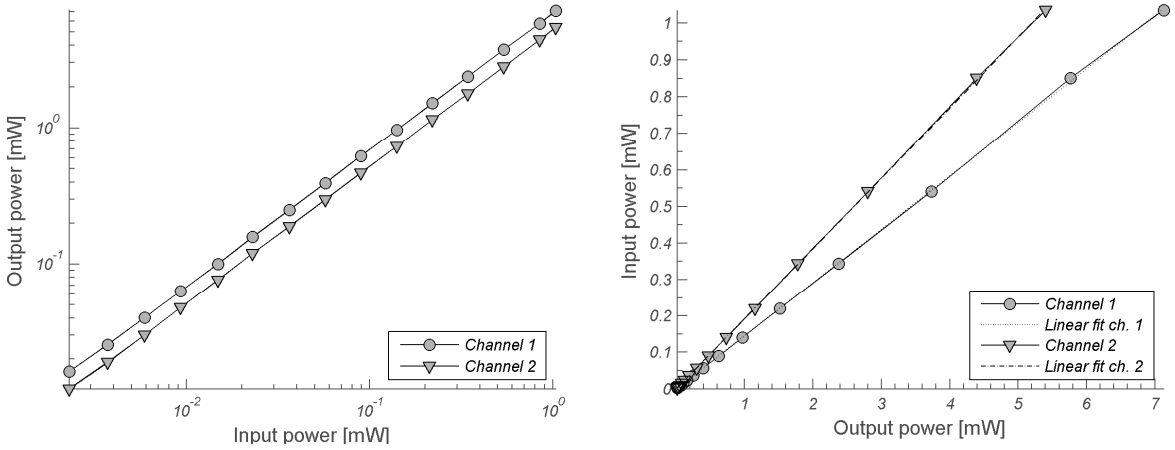

Figure 2 - Input vs. output power for channels 1-2

Different values for all parameters above were calculated for all measurements, for the different power meter readings. The parameters for different measurements were averaged to find values suitable for later use. These averaged values are given in Table 3.

Table 3 - parameters for channels 1 and 2

	OFFSET *I* [MV]	OFFSET *Q* [MV]	ANGLE φ [RAD]	NORMALISATION *N*	LINEAR SLOPE
Channel 1	0.310875	-7.312922	0.050447	0.983457	0.145958
Channel 2	1.937075	-5.314815	0.054926	0.975364	0.192418

The slope values in Table 3 come from the linear fits, and can be used to find the input powers from the output powers with the formula (*input power*) = (*slope*) × (*output power*).

Calibration of channels 3 to 8

For the remaining channels, one measurement was taken for each channel at an input power of 10 dBm from the synthesizer. 2 channels were measured at a time, and the power meter readings for the measurements are given in Table 4.

Table 4 - Power meter readings for channels 3 to 8

	CHANNEL 3 AND 4	CHANNEL 5 AND 6	CHANNEL 7 AND 8
Power meter readings [dBm]	-16.15	-15.96	-15.74

The signal curves for these measurements were also truncated to an integer number of periods, as for channels 1 and 2. Then the offsets, angles and normalisations were found for each channel, but no averaging was done since only one measurement was taken per channel. The parameters are given for all 8 channels in Table 5.

Table 5 - Parameters for channels 1 to 8

	OFFSET *I* [MV]	OFFSET *Q* [MV]	NORMALISATION *N*	ANGLE φ [RAD]
Channel 1	0.310875	-7.312922	0.983457	0.050447
Channel 2	1.937075	-5.314815	0.975364	0.054926
Channel 3	-2.365806	-6.697663	0.972546	0.059230
Channel 4	-5.778431	-10.990651	0.980979	0.047808
Channel 5	0.001812	-8.927038	0.986188	0.065593
Channel 6	0.149879	-8.363992	0.984704	0.059688
Channel 7	-2.507403	-10.753497	0.968075	0.054181
Channel 8	-0.771075	-4.562091	0.972296	0.069121

The offsets for the *I* and *Q* channels, the normalisations and the angles are all shown in Figure 3 for 10 dBm from the synthesizer. In addition, the output power is plotted versus the input power for all 8 channels in the same figure. The normalisations, angles and offsets are averaged for channels 1 and 2, and the error bars represent the standard deviations in those channels. As seen from the plots, the normalisation factors, angles and offsets all have reasonable values. However, channels 5 and 6 have a quite different ratio between the power in and the power out than the others. Therefore it is recommended to prioritize the other channels first.

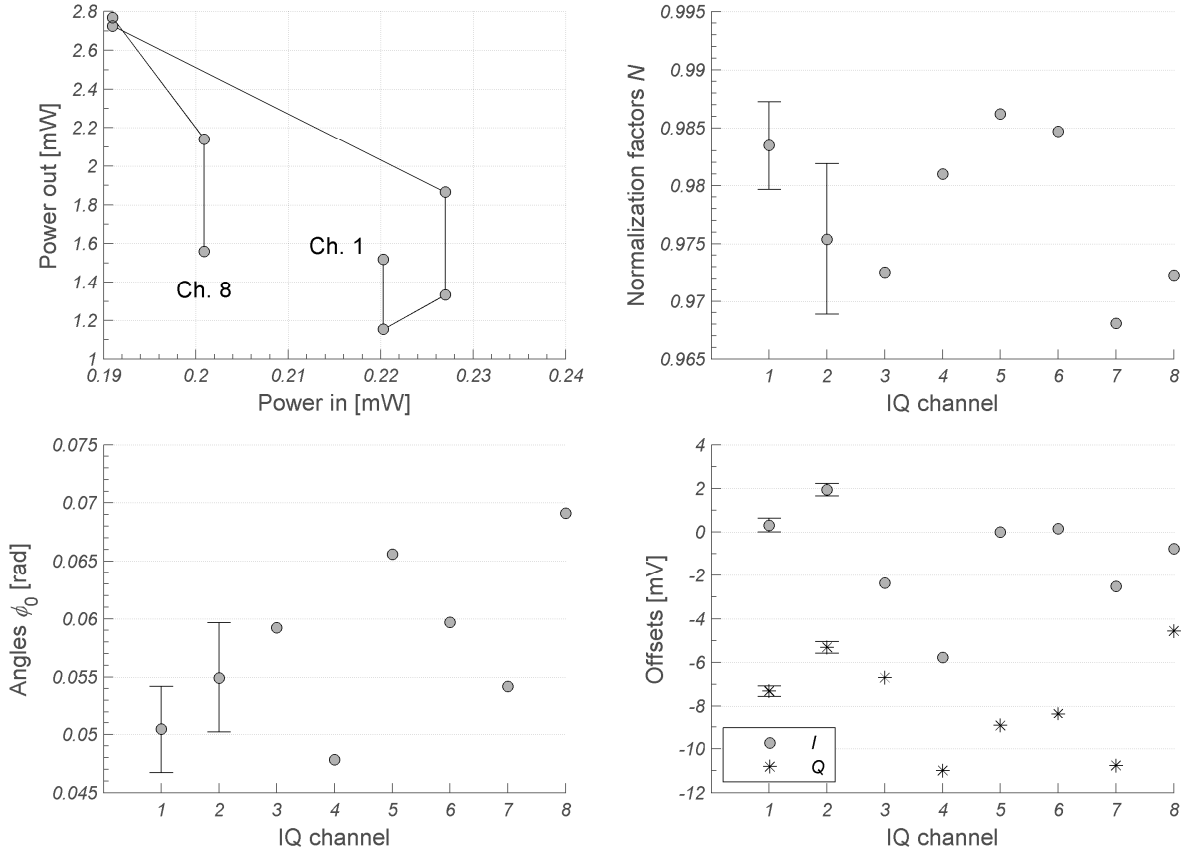

Figure 3 - Upper left: Power out vs. power in for all 8 channels at 10 dBm from the synthesizer. Upper right: Normalisation factors. Lower left: Angles. Lower right: Offsets for *I* and *Q* channels

Appendix C

Collection of publications

This appendix contains two articles in which the author made contributions during the project.

The first article is named 'Experimental Program for the CLIC Test Facility 3 Test Beam Line', and was presented at the first International Particle Accelerator Conference (IPAC'10). The article describes the TBL, with the challenges of beam transport and the planned experiments.

The second article is named 'Commissioning Status of the Decelerator Test Beam Line in CTF3', and was presented at the 25th Linear Accelerator Conference (LINAC'10). This article provides a summary of the first experimental results, e.g., the GUI presented in Chapter 4 and power production experiments as described in Section 5.1.

EXPERIMENTAL PROGRAM FOR THE CLIC TEST FACILITY 3 TEST BEAM LINE*

E. Adli†, University of Oslo, Oslo, Norway, A.E. Dabrowski, S. Döbert,
M. Olvegård, D. Schulte, I. Syratchev, CERN, Geneva, Switzerland
R. L. Lillestøl, NTNU, Trondheim, Norway

Abstract

The CLIC Test Facility 3 Test Beam Line is the first prototype for the CLIC drive beam decelerator. Stable transport of the drive beam under deceleration is a mandatory component in the CLIC two-beam scheme. In the Test Beam Line more than 50% of the total energy will be extracted from a 150 MeV, 28 A electron drive beam, by the use of 16 power extraction and transfer structures. A number of experiments are foreseen to investigate the drive beam characteristics under deceleration in the Test Beam Line, including beam stability, beam blow up and the efficiency of the power extraction. General benchmarking of decelerator simulation and theory studies will also be performed. Specially designed instrumentation including precision BPMs, loss monitors and a time-resolved spectrometer dump will be used for the experiments. This paper describes the experimental program foreseen for the Test Beam Line, including the relevance of the results for the CLIC decelerator studies.

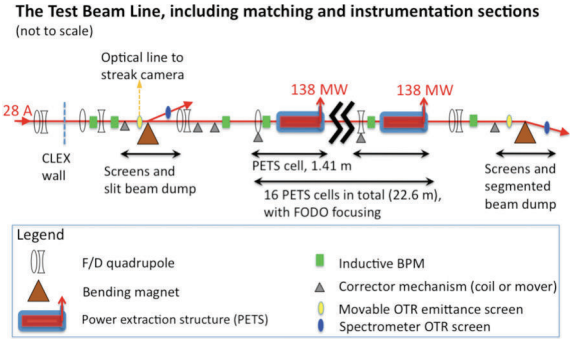

Figure 1: Functional sketch of the Test Beam Line. The line consists of 8 FODO cells, with 16 PETS in total. Matching and instrumentation sections providing emittance and energy measurement, are installed at the start and the end of line.

INTRODUCTION

The Test Beam Line (TBL) will be the first demonstration of the decelerator for the Compact Linear Collider (CLIC) [1]. In the CLIC decelerator 84% of the energy will be extracted from a 101 A electron drive beam, while in the TBL about 54% of the energy will be extracted from a 28 A electron beam. The drive beam in both the CLIC decelerator and TBL will be decelerated by the 12 GHz fundamental mode in a number of constant impedance power extraction structures (PETS) [2]. The high group velocity of this mode will induce a high-energy transient head of the beam, of length of the order of 1 ns. The deceleration of the steady state part will also vary significantly due to the 12 GHz mode frequency combined with the 1 mm rms bunch length. Because the sole purpose of the CLIC drive beam is to provide stable, uniform and efficient rf power for the main beam, particles of all energies must be transported equally well towards the end of the lattice. A FODO lattice is chosen for focusing, due to the large energy acceptance. The gradient of the quadrupoles will be adjusted to provide constant phase-advance per cell for the most decelerated particles.

The TBL consists of 16 cells each containing a 0.8 m long PETS, one quadrupole on mover and one inductive beam position monitor (BPM). It is installed in the CLIC Test Facility 3 Experimental Area (CLEX) [3], which provides the drive beam. Instrumentation and matching sections, to be described later, are installed before and after the TBL. The layout of the TBL is shown in Figure 1, including the location of key instrumentation. The length of the TBL PETS are 3.7 times longer than the CLIC PETS, allowing the TBL PETS to reach a power production slightly above the CLIC baseline of 135 MW, despite the 3.6 times lower drive beam current. For the nominal CLEX beam current of 28 A, this results in a total peak deceleration of about 84 MeV. Figure 2 illustrates the PETS induced energy spread in the first 4 ns of the TBL beam. See Table 1 for a comparison between TBL and CLIC decelerator parameters.

The main purposes of the TBL are 1) to show stable power production in 16 PETS, and to correlate the rf power output with energy loss and theoretical predictions, 2) to demonstrate stable beam transport while converting more than 50% of the electron energy to 12 GHz rf power and 3) to act as a test-bench for decelerator beam-based alignment schemes. In addition the TBL will provide valuable benchmarking of simulation codes and decelerator hardware. In this paper we describe in more detail the different purposes of the TBL and the expected performance, followed by a discussion of the instrumentation installed in order to acquire the necessary beam observables.

POWER PRODUCTION AND ENERGY LOSS

It is important to understand and measure with good precision the drive beam deceleration in the TBL. The energy loss of the beam can be 1) predicted by the incoming beam characteristics, 2) deduced from the rf power produced or 3) measured directly. The three different calculations will

* Work supported by the Research Council of Norway.
† Erik.Adli@cern.ch

Table 1: TBL versus CLIC parameters

Parameter	Symbol	TBL	CLIC
Number of PETS [-]	N_{PETS}	16	1492
Length of PETS [m]	L_{PETS}	0.80	0.21
Initial average current [A]	I_0	28	101
Power per PETS [MW]	P	∼138	135
Initial energy [MeV]	E_0	150	2400
Mean energy extracted [%]	η_{extr}	∼54	84
PETS sync. freq. [GHz]	f_{rf}	12	12
Number of FODO cells [-]	N_{FODO}	8	524
Length of FODO cells [m]	L_{FODO}	2.82	2.01
Pulse length [ns]	t_{pulse}	140	240
Transient length [ns]	t_{fill}	3	1
Bunch rms length [mm]	σ_{z}	1.0	1.0
Init. norm. emittance [μm]	$\epsilon_{\mathrm{N\,x,y}}$	150	150
Beam pipe radius [mm]	a_0	11.5	11.5

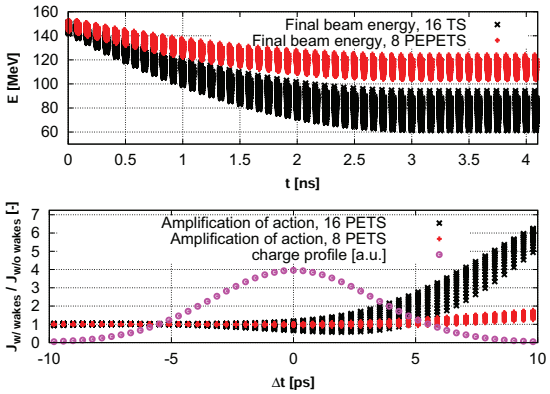

Figure 2: The upper plot shows the beam energy after deceleration (8 and 16 PETS, first 4 ns of pulse). For 16 PETS the leading particle is about 2.3 times more energetic than minimum energy particle. The lower plot shows the amplification of macro particle action due to the dipole wake for an offset beam, within a bunch in the steady-state part of the beam (8 and 16 PETS).

be correlated, and we aim to achieve correlation of the calculations to an accuracy of the order of 10%. The predicted power generation in a PETS depends on the beam intensity I and the form-factor F(λ) as $P \propto I^2 F^2(\lambda)$. In the case of a detuning between bunch and resonant frequency, Δf, power production is further reduced by a factor $P \propto \frac{1-\cos(2\pi t_{\mathrm{fill}}\Delta f)}{1-\cos(2\pi\Delta f/f_{\mathrm{rf}})}/(t_{\mathrm{fill}}f_{\mathrm{rf}})^2$, to first order.

A long optical line will transport Optical Transition Radiation (OTR) from a screen at the beginning of the TBL to a streak camera for bunch length ($<$ 1 ps resolution) and bunch spacing measurements (2-3 ps resolution). An RF pickup, based on power measurements of higher order harmonics of 12 GHz will, once calibrated with the streak camera measurement, provide an online monitoring of the bunch form factor along the pulse train. The BPMs will measure the beam intensity with an accuracy of about 1%. Two spectrometers will be equipped with OTR screens for integrated average energy and energy spread measurements at the beginning and end of the TBL. A segmented beam dump, installed in the final spectrometer, will provide a time resolved (ns) energy spread measurement, with an accuracy estimated to about 5% [4]. The rf measurements accuracy will be limited by the fact that the 138 MW PETS output signal needs to be attenuated by about 90 dB, and we expect a measurement accuracy of 10%.

For a perfectly constructed PETS the power production is expected to be independent of the beam offset, to first order. Dedicated tests will be performed to correlate the 12 GHz power production with the beam offset, using the prototype PETS [5] where the signals from the directional couplers at each side of the PETS can be measured independently.

TRANSPORT OF DECELERATED BEAM

The beam envelope is estimated to grow mainly due to adiabatic undamping, wake fields and misalignment [1]. For a perfect incoming beam and perfect injection, the 3σ beam envelope in the TBL will reach 2/3 of the aperture. The TBL envelope is more than a factor of two larger than for CLIC, from this point of view yielding a more challenging transport in the TBL. An estimation of the amplification of a trailing point-like particle due to the dipole wake from a leading particle can be estimated as $\Upsilon \sim \int ds \frac{W'(s)\beta(s)q_b}{E(s)}$ [6], where W' is the wake amplitude, β the beta function, q_b the bunch charge and E the energy, all taken at location s. This yields $\Upsilon_{\mathrm{CLIC}}/\Upsilon_{\mathrm{TBL}} \approx 7$. Thus, we expect the effects of the multibunch dipole wakes to be much less significant for the TBL than for CLIC. Calculations of the single-bunch wakes show, however, that a small fraction of macro particles towards the end of the bunches increase their transverse action by several factors in the case of injection offset, see Figure 2 (similar values are obtained for CLIC). Assuming all 16 PETS are installed with SiC damping material for higher-order mode damping, beam dynamics simulations show that the dipole wakes should not significantly impede beam transport, for reasonable values of beam injection and misalignment [1]. It is however of interest to provoke an observation of wake effects in order to benchmark the simulations. The only potentially directly observable effect we predict from the dipole wake is an increase in emittance, measured on the final emittance screen, when the beam is injected with a significant offset. For the nominal TBL parameters we estimate 10-15% increase in the rms beam size, for an injection offset of one σ, which we expect to be challenging to disentangle from other effects. Most of the emittance growth occurs towards the end of the line, thus most of the PETS would have to be installed in order to observe an eventual emittance growth due to wakes. One way to achieve direct observations of the transverse wake effects could be to use resonant kickers to introduce beam jitter at a specific frequency before the TBL, and measure the amplification of the jitter at the

end, as suggested in [7]. However, this equipment is not in the current baseline for the TBL.

Two movable OTR emittance screens, indicated in Figure 1, will be installed in order to measure the emittance growth resulting from filamentation and wake fields. The screens will also be used to measure beam ellipse parameters for matching into the periodic lattice and into the final spectrometer. Cerenkov light based loss monitors for the TBL are currently being studied, and a prototype is expected to be tested in the TBL in 2010 [8].

DEMONSTRATION OF DECELERATOR ALIGNMENT

The 1 km CLIC decelerator sectors contain one quadrupole per meter in order to provide strong focusing for dipole wake mitigation [1]. Due to quadrupole misalignments, the beam envelope might increase by an order of magnitude, and because of the large energy spread, 1-to-1 steering into BPMs might not ensure sufficient orbit control for particles of all energies. As alternative, an orbit correction scheme based on dispersion-free steering, varying the average pulse intensity using the CLIC delay loop [9] and exploiting the PETS beam loading, is proposed. The scheme shows excellent performance by simulation [10]. However, due to its novelty it is crucial that the scheme be tested under realistic conditions. In the TBL the decelerator scheme will be tested, exploiting the CTF3 delay loop to vary the average pulse intensity. We aim to perform the dispersion-free steering within a single pulse of 140 ns.

Inductive BPMs [11] with a position resolution of 5 μm will enable measurement of the orbit with precision similar to what is required for the decelerator, and the analog and digital bandwidth ensure spatial resolution of < 10 ns. As orbit correctors, specially designed quadrupole movers [12] with a precision of 5 μm will be used.

SCHEDULE

By spring 2010 all dipole magnets, quadrupole magnets and quadrupole movers and one PETS have been installed. A power production of almost 20 MW has been achieved by a drive beam of around 10 A. Two to three additional PETS are scheduled for installation in 2010, a total of nine PETS by the spring of 2011, and all 16 PETS by the end of 2011. The end-of-line segmented spectrometer dump is under production and scheduled for installation in Autumn 2010 [4]. In 2010 the line will be further commissioned with up to four PETS installed, and correlations between beam offset and power production will be measured. Correlations between total rf power produced and total energy loss are planned using the segmented dump. In 2011 the commissioning will continue with 8-9 PETS (up to 30% rf power extraction), and by 2012 the line should be fully commissioned and demonstrate stable power production and beam transport with more than 50% rf power extraction. Once stable beam transport is achieved, alignment experiments may start. The dispersion-free steering should be performed with 16 PETS in order to provide a convincing demonstration for the decelerator, however the principle could be demonstrated with fewer PETS. Rf processing time of the PETS might be a concern, as there is currently no plan to pre-condition the PETS before installation. For the PETS tested in the ASTA test-bench at SLAC [13] in the order of 10^7 rf pulses were needed before reaching the nominal power production of 135 MW at low break down rate, while for the Two-beam Test Stand tests in CTF3 in the order of 10^5 beam pulses were needed in order to reach a power level of > 135 MW [13]. However, the full TBL program can be completed with a relatively high break down rate with respect to the CLIC target of 10^{-7}, thus a relatively smaller number of pulses may be needed for processing before experimentation can start.

ACKNOWLEDGEMENTS

The Test Beam Line experiment is built and operated by CERN within an international collaboration; beam physics studies are performed by the University of Oslo, the PETS prototype and the quadrupole movers are provided by CIEMAT, Madrid, BPMs by IFIC, Valencia and BPM electronics by UPC, Barcelona and LAPP, Annecy.

CONCLUSIONS

The Test Beam Line will provide the first demonstration of the CLIC decelerator. We aim to show stable beam transport while converting more than 50% of the electron drive beam energy into rf power, using CLIC baseline PETS structures operating at least at the CLIC nominal power production level of 135 MW. The effect of transverse wakes is expected to be significantly smaller in the TBL than in the decelerator. If the rf simulations for the baseline PETS structure are accurate, direct observations of the transverse wakes will be challenging to observe with the available instrumentation. Beam-based alignment schemes specially devised for the CLIC decelerator are planned to be demonstrated in the TBL once stable beam transport and power production have been shown.

REFERENCES

[1] E. Adli, Ph.D. thesis, University of Oslo, Oslo, 2009
[2] I. Syratchev et al., PAC'07, Albuquerque, 2007, p. 2194
[3] G. Guignard (ed.), CERN, Geneva (2000) CERN 2000-008
[4] M. Olvegård et al. these proceedings, MOPE060
[5] F. Toral et al., these proceedings, THPEA041
[6] D. Schulte, PAC'09, Vancouver, 2009, FR5RFP055
[7] D. Schulte and I. Syratchev, PAC'05, Knoxville, TN, 2005, p. 1177
[8] A. Intermite et al., BIW'10, Santa Fe, 2010, TUPSM046
[9] D. Schulte, LINAC'00, Monterey, CA, 2000, p. 726
[10] E. Adli and D. Schulte EPAC'08, Genoa, 2008, p. 547
[11] J.J. Garcia-Garrigos et al., EPAC'08, Genova, 2008, p. 1110
[12] F. Toral et al., EPAC'08, Genova, 2008, p. 1517
[13] I. Syratchev et al., PAC'09, Vancouver, 2009, WE3RAC02

COMMISSIONING STATUS OF THE DECELERATOR TEST BEAM LINE IN CTF3

E. Adli, S. Döbert, R. Lillestol, M. Olvegaard, I. Syratchev, CERN, Geneva, Switzerland
D. Carrillo, F. Toral, CIEMAT, Madrid, Spain
A. Faus-Golfe, J.J. Garcia-Garrigos, IFIC (CSIC-UV), Valencia, Spain.
Yu. Kubyshin, G.Montoro, UPC, Barcelona, Spain

Abstract

The CLIC Test Facility (CTF3) at CERN was constructed by the CTF3 collaboration to study the feasibility of the concepts for a compact linear collider. The test beam line (TBL) recently added to the CTF3 machine was designed to study the CLIC decelerator beam dynamics and 12 GHz power production. The beam line consists of a FODO lattice with high precision BPM's and quadrupoles on movers for precise beam alignment. A total of 16 Power Extraction and Transfer Structures (PETS) will be installed in between the quadrupoles to extract 12 GHz power from the drive beam provided by the CTF3 machine. The CTF3 drive beam with a bunch-train length of 140 ns, 12 GHz bunch repetition frequency and an average current over the train of up to 28 A will be injected into the test beam line. Each PETS structure will produce 135 MW of 12 GHz power at nominal current. The beam will have lost more than 50 % of its initial energy of 150 MeV at the end of the beam line and will contain particles with energies between 65 MeV and 150 MeV. The beam line is completely installed and the PETS structures will be successively added until the end of 2011. The paper will describe the first results obtained during commissioning of the beam line and the first PETS prototype.

INTRODUCTION

In CLIC decelerator a 101 A beam will be decelerated from 2.4 GeV down to 240 MeV converting 85 % of its energy into 12 GHz microwave power. The power will be extracted by power extraction and transfer structures (PETS). In order to demonstrate the feasibility of the CLIC decelerator a special test beam line (TBL) has been implemented into CTF3 at CERN. The line will have 16 PETS installed in its final stage. Table 1 lists the parameters of the CLIC decelerator and of TBL in CTF3 for comparison. Each PETS in TBL will produce the nominal CLIC power of 135 MW with a beam current of 28 A . The PETS in TBL are a factor 4 longer compared to CLIC to compensate for the lower drive beam current in CTF3. The initial energy for the decelerator of CTF3 is even lower than the final energy for CLIC which makes the experiment more difficult in this respect. On the other hand wakefield effects will be less pronounced in TBL due to the much shorter beam line. The emphasis for the experimental program of TBL [1] will be on 12 GHz power production and the transport of the decelerated beam. It is essential for CLIC that the 12 GHz power production is efficient and stable. Therefore measurements of the energy balance of the produced rf power and the energy loss of the beam will be carried out. The stability of the produced power both in amplitude and phase will be determined. The beam transport is challenging because the beam develops a large energy spread during deceleration. The difference in deceleration for the most and least declerated particles amounts up to 85 MeV once the line is equipped with 16 PETS. The beam envelope is increasing along the beam line and will fill 2/3 of the aperture in the case of TBL assuming perfect alignment. The alignment of the quadrupoles of the FODO lattice and the PETS itself is critical for full transmission. The quadrupoles have been installed on moving tables developed by CIEMAT [2] which allow a positioning in the micrometer range. Beam based alignment studies are foreseen using the precision BPM's developed by IFIC Valencia and UPC Barcelona [3].

Table 1: Comparison of beam parameters for CLIC and TBL.

Parameter	Symbol	TBL	CLIC
Number of PETS [-]	N_{PETS}	16	1492
Length of PETS [m]	L_{PETS}	0.80	0.21
Initial average current [A]	I_0	28	101
Power per PETS [MW]	P	$\sim$138	135
Initial energy [MeV]	E_0	150	2400
Mean energy extracted [%]	η_{extr}	$\sim$54	84
PETS sync. freq. [GHz]	f_{rf}	12	12
Number of FODO cells [-]	N_{FODO}	8	524
Length of FODO cells [m]	L_{FODO}	2.82	2.01
Pulse length [ns]	t_{pulse}	140	240
Transient length [ns]	t_{fill}	3	1
Bunch rms length [mm]	σ_z	1.0	1.0
Init. norm. emittance [μm]	$\epsilon_{\mathrm{N\,x,y}}$	150	150
Beam pipe radius [mm]	a_0	11.5	11.5

The beam line has been installed in CTF3 comprising the FODO lattice, the precision BPM's and a PETS prototype. This first PETS has been developed and fabricated in collaboration with CIEMAT [4]. Each PETS consists of 8 copper bars machined to high precision which are clamped together with an extraction coupler and installed in a vacuum tank. So far only one prototype PETS tank has been installed and the production of a series of 8 more tanks is currently under way. A diagnostic section has been installed in front of and at the

end of the line to measure transverse beam parameters and the energy spectrum. A time resolved spectrometer has been developed to observe the particular energy profile of the decelerated beam [5]. Figure 1 shows a photo of the TBL line installed in CTF3.



Figure 1: Photo of the test beam line in CTF3.

FIRST RESULTS

The commissioning of the beam line and the instrumentation started with a 3 GHz beam between 2 and 3 A. The energy of the beam was 113 MeV instead of the nominal 150 MeV planned for TBL. The Twiss-parameters of this beam have been measured using an OTR screen in front of TBL. The obtained beam parameters have been used to calculate a matching of the incoming beam to the FODO lattice. The matched beam could be transported through one PETS to the end of the line. A graphical user interface has been developed to ease this kind of operation. This application monitors the beam currents and positions along the line and calculates the matching for different phase advances of the lattice and sets the quadrupoles to their new values. The matching is done always for the particles with the lowest energy. A screen shot of the interface is shown in figure 2.

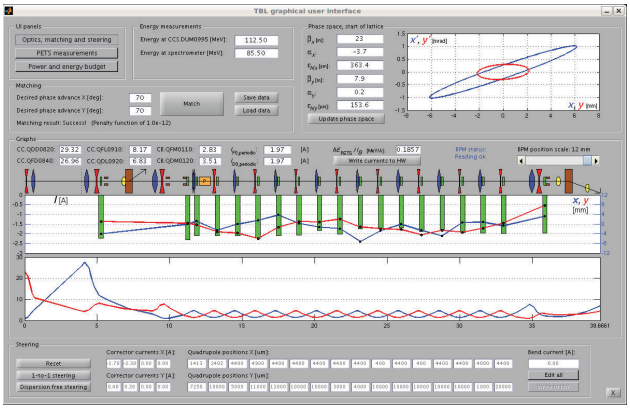

Figure 2: Graphical user interface showing the beam transmission and trajectory as well as the beta functions of the matched beam.

The beginning of the commissioning focused on the power production with the prototype PETS tank. The power produced in the PETS is proportional to the square of the beam current and the form factor determined by the bunch length $P \propto I^2F^2$. More details on the theory of the power production can be found in [6]. The power is extracted in a symmetrical coupler to two WR90 waveguides equipped with directional couplers and high power loads. The 12 GHz signal is subsequently mixed down to base band and detected by IQ-demodulators. The 12 GHz power produced by the beam agrees well with the theoretical predictions. Figure 3 shows an example of the measured rf signals together with the prediction from the BPM signal directly after the PETS as well as the phase of the rf signals. In this example a 12 GHz combined beam of 8 A was used and a form factor of 0.83 was used for the prediction. In CTF3 a 3 GHz beam from the linac can be combined using the combiner ring into a beam with a four times higher current and a 12 GHz bunch spacing [7]. The bunch length was not measured directly but is within the expected range for the CTF3 beam [8]. The phase measurement shows a dip along the bunch train which comes from the beam and is due to the rf pulse compression used in CTF3. The shape and phase of the extracted 12 GHz power is an excellent and very sensitive diagnostics for the quality of the drive beam production and combination. Shaping the rf power pulse correctly will be one of the experiments done in TBL to demonstrate the CLIC decelerator. The maximum power produced so far was 20 MW with a beam current of 10 A with no sign of breakdown.

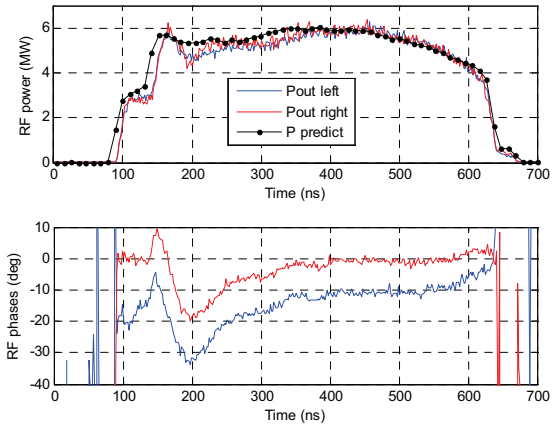

Figure 3: PETS output power measurement and prediction from the BPM signal (upper) and the corresponding phase of the rf signal (lower).

The inductive BPM's developed for TBL have been designed to have a 5 µm resolution in order to insure the beam-based alignment requirements. The quadrupoles have to be aligned within 10 µm by beam-based alignment to insure proper beam transport through the line once equipped with 16 PETS. A first measurement of the BPM resolution measuring the trajectory of the beam in three consecutive BPM's to take out the effects of beam jitter has been performed. For a beam with 2.3 A

average current 57 μm resolution was measured corresponding well to the specified resolution of 5 μm for the nominal beam current of 28 A. The resolution was determined as the rms value of the difference distribution of the measured beam position in the middle BPM and the predicted beam position from the two other BPM's. However the BPM signals suffered from additional noise coming from beam losses.

Each quadrupole is mounted on a moving table allowing ±4 mm horizontal and vertical movement with a precision of 5 μm. The tables can be moved with a resolution of 1 μm. The movers have been used for kick measurements to verify the optics in the beam line systematically along the line. Figure 4 shows an example of such a measurement. Here the first quadrupole was moved to kick the beam and the measured trajectory was compared to the theoretical optics model. The first quadrupole was moved by 1 mm in horizontal direction for this example. The agreement is good and identifies a problem at the position of BPM 13 which will be corrected.

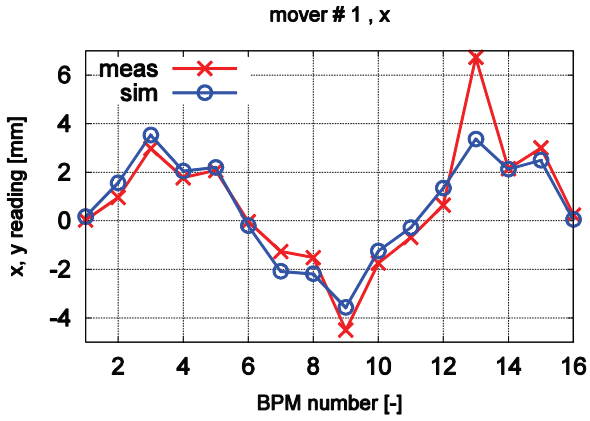

Figure 4: Kick measurement using the mover of the first quadrupole in the horizontal plane. The measured beam trajectory is compared to the optics simulations.

Finally the diagnostic sections in front of TBL and at the end of the beam line have been commissioned. Each diagnostic section is equipped with an OTR screen and a CCD camera allowing emittance and Twiss-parameter measurements using quadrupole scans. The energy and energy-spread can be measured before and after the line with a spectrometer dipole magnet and an OTR screen in the dispersive section. In addition the spectrometer at the end of the line is equipped with a slit dump which allows a time resolved energy spread measurement. This device will be replaced by a segmented dump which will enable single shot time resolved energy spread measurements. During commission the Twiss parameters of the beam have been measured and used to match the beam to the periodic FODO optics. The beam parameters have been measured subsequently at the end of the line and were found to be consistent with the predictions of the optics simulations. An energy spread of 2.5% FWHM was measured at the end of the line consistent with measurements in the CTF3 linac.

CONCLUSIONS

The commissioning of the test beam line in CTF3 dedicated to demonstrate the feasibility of the CLIC decelerator has been successfully started. A first PETS prototype has been manufactured and tested with beam. The produced 12 GHz output power corresponds well to the theoretical predictions. Until now a maximum of 20 MW of rf power could be extracted from the beam. The fully combined 28A drive beam of CTF3 is necessary to reach the goal of 135 MW extracted power. We plan to demonstrate the full power production by the end of this year. The series production of 8 more PETS tanks is underway and we plan to install those by the beginning of 2011.

The beam optics and diagnostics developed for TBL have been commissioned with different types of beams. The micrometer quadrupole movers have been used successfully for kick measurements to verify the beam optics. No major problems have been found with the optics.

A first resolution measurement of the inductive BPM gave a satisfactory result but can still be improved. At the end of the beam line a time resolved spectrometer using a slit dump has been installed and commissioned. This diagnostic will allow to bench mark the deceleration process in the PETS structures.

In 2011 the line will be used with 8 PETS installed and we plan to complete the line with a total of 16 deceleration structures in 2012.

REFERENCES

[1] E. Adli et al. ,'Experimental Program for the CLIC Test Facility 3 Test Beam Line', IPAC 2010, Kyoto, Japan

[2] F. Toral et al.,'Design, Manufacturing and tests of a micrometer precision mover for CTF3 quadrupoles', EPAC 08, Genova, Italy 2008.

[3] J.J. Garcia Garrigos, 'Design and Construction of a Beam Position Monitor Prototype for the Test Beam Line of the CTF3', Thesis, Universitat Politecnica de Valencia, Spain 2008

[4] F. Toral et al.,'Manufacturing and Testing of a TBL PETS Prototype', IPAC 2010, Kyoto, Japan

[5] M. Olvegard et al.,'Spectrometry in the Test Beam Line at CTF3', IPAC 2010, Kyoto, Japan

[6] E. Adli, Ph.D. thesis, University of Oslo, Oslo, Norway 2009

[7] P.K. Skowronski, 'Progress towards the CLIC feasibility demonstration in CTF3', IPAC 2010, Kyoto, Japan

[8] A.E. Dabrowski et al.,'Measuring the longitudinal bunch profile at CTF3', this conference

Appendix D

Extra figures

Because Figures 4.1 and 4.2 contain a lot of details which may be difficult to see, they are presented here in larger formats.

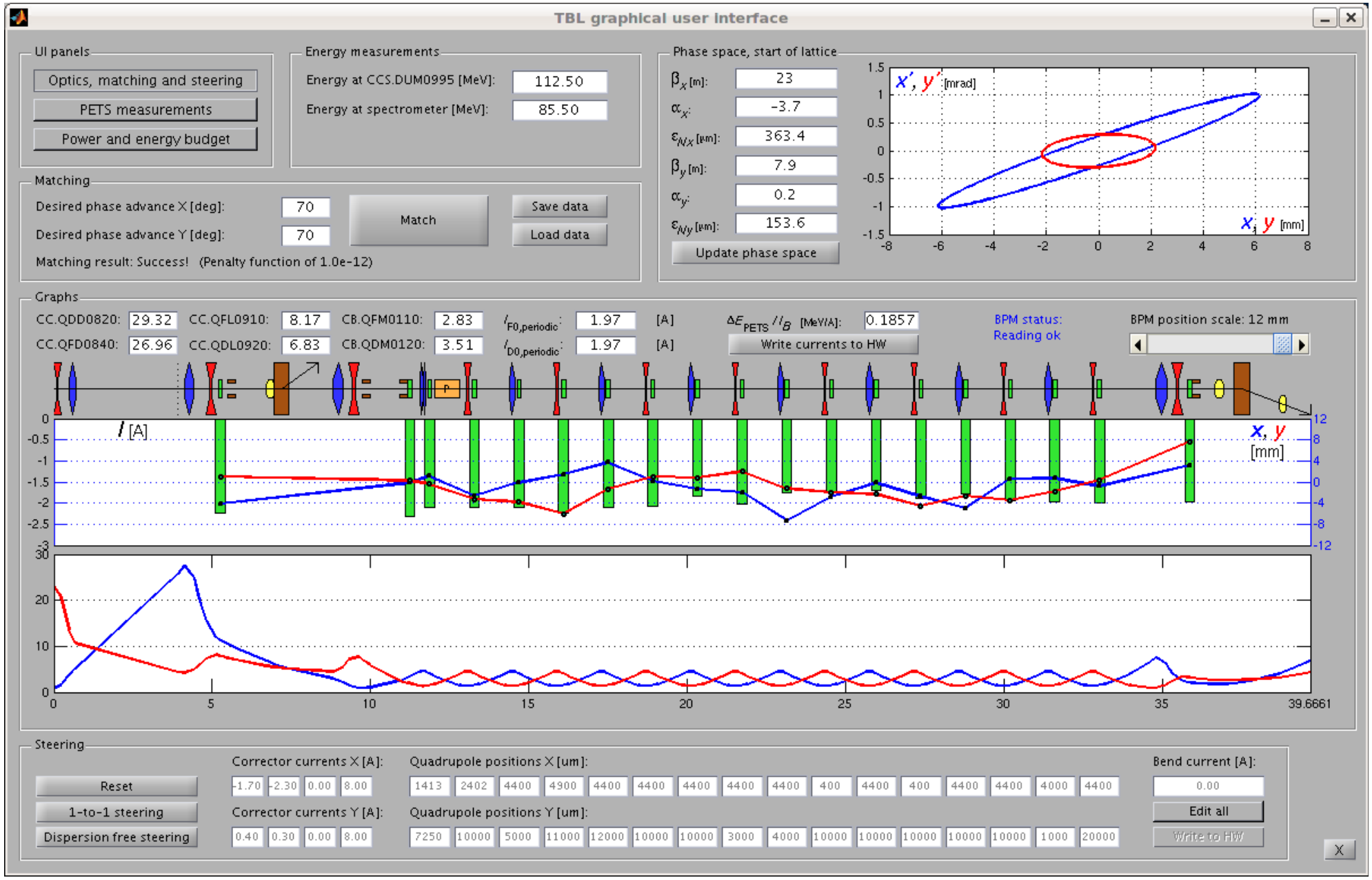
TBL graphical user interface
UI panels
Optics, matching and steering
PETS measurements
Power and energy budget
Energy measurements
Energy at CCS.DUM0995 [MeV]: 112.50
Energy at spectrometer [MeV]: 85.50
Phase space, start of lattice
βx [m]: 23
αx: -3.7
εNx [μm]: 363.4
βy [m]: 7.9
αy: 0.2
εNy [μm]: 153.6
Update phase space
x', y' [mrad]
x, y [mm]
Matching
Desired phase advance X [deg]: 70
Desired phase advance Y [deg]: 70
Match
Save data
Load data
Matching result: Success! (Penalty function of 1.0e-12)
Graphs
CC.QDD0820: 29.32
CC.QFD0840: 26.96
CC.QFL0910: 8.17
CC.QDL0920: 6.83
CB.QFM0110: 2.83
CB.QDM0120: 3.51
IF0,periodic: 1.97 [A]
ID0,periodic: 1.97 [A]
ΔEPETS / IB [MeV/A]: 0.1857
Write currents to HW
BPM status:
Reading ok
BPM position scale: 12 mm
I [A]
x, y [mm]
39.6661
Steering
Reset
1-to-1 steering
Dispersion free steering
Corrector currents X [A]: -1.70 -2.30 0.00 8.00
Corrector currents Y [A]: 0.40 0.30 0.00 8.00
Quadrupole positions X [um]: 1413 2402 4400 4900 4400 4400 4400 4400 4400 400 4400 400 4400 4400 4000 4400
Quadrupole positions Y [um]: 7250 10000 5000 11000 12000 10000 10000 3000 4000 10000 10000 10000 10000 10000 1000 20000
Bend current [A]: 0.00
Edit all
Write to HW
X

TBL graphical user interface

UI panels

Optics, matching and steering

PETS measurements

Power and energy budget

Predicted values

$F(\lambda)$: 0.97

Δf [MHz]: 0

$$\frac{1}{4}(R'/Q)\frac{\omega_{rf}}{v_g}L_{PETS}^2 I^2 F^2(\lambda)\eta_{\Omega,PETS}^2\frac{1}{(\tau_{fill}f_{rf})^2}\frac{1-cos(2\pi\tau_{fill}\Delta f)}{1-cos(2\pi\Delta f/f_{rf})}$$

PETS predicted output power [MW]: 25.19

Predicted energy loss per PETS [MV]: 2.207

Update prediction from parameters in file

BPM and RF signals

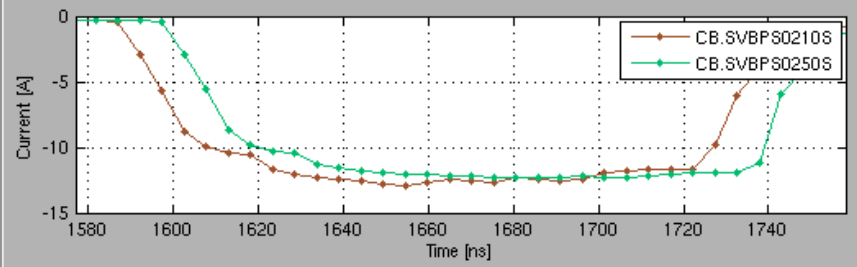

Measured PETS output power, left arm [MW]: 11.55 Refl. power, left [MW]: 0.098

Measured PETS output power, right arm [MW]: 13.65 Refl. power, right [MW]: 0.039

Measured PETS output power, total [MW]: 25.36

Mean current at CB.STBPS0210S [A]: −12.37

Mean current at CB.STBPS0250S [A]: −11.57

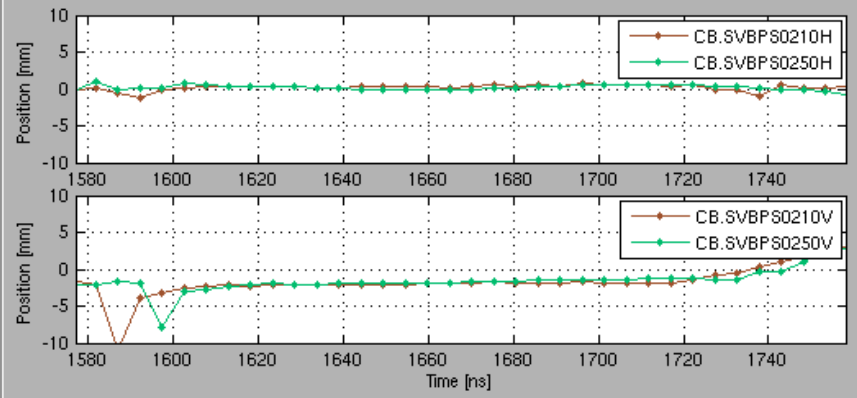

Save number of pulses: 300 Save Saving Pulses... 145/300

Beam position within the first PETS

Wanted offset X [mm]: 0

Wanted offset Y [mm]: 2

Radial offset [mm]: 2.000

Write desired offset to HW

PETS Aperture radius: 11.5 mm



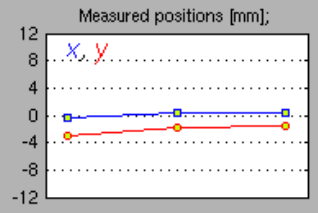

X:	-0.186	0.351	0.111
Y:	-3.006	-1.888	-1.616

Power production

$F(\lambda)$: 0.97

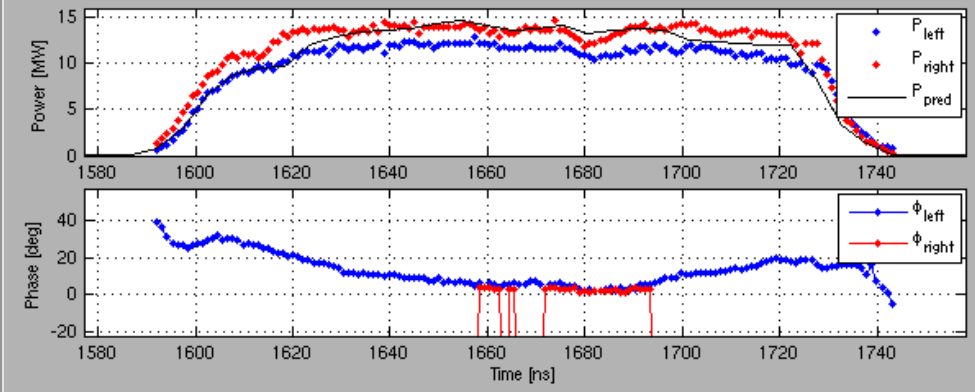

X